Article

Neuron

# The Mouse Cortical Connectome, Characterized by an Ultra-Dense Cortical Graph, Maintains Specificity by Distinct Connectivity Profiles

## Highlights

- Retrograde tracer injections are restricted to single areas in mouse cortex
- Individual areal maps for each brain are used for location of labeled neurons
- 97% of all possible cortico-cortical connections exist
- Areas are characterized by weight-specific connectivity profiles

## Authors

Răzvan Gămănuţ, Henry Kennedy, Zoltán Toroczkai, Mária Ercsey-Ravasz, David C. Van Essen, Kenneth Knoblauch, Andreas Burkhalter

## Correspondence

henry.kennedy@inserm.fr (H.K.), burkhala@wustl.edu (A.B.)

## In Brief

Gămănuţ et al. investigate anatomical cortico-cortical connections in the mouse at the meso-scale level and show that almost all possible connections exist. Efficiency of the network and specificity of the connections are ensured by the existence of weighted connectivity profiles.

Gămănuţ et al., 2018, Neuron *97*, 698–715
February 7, 2018 
https://doi.org/10.1016/j.neuron.2017.12.037

CellPress

CellPress

Neuron
Article

# The Mouse Cortical Connectome, Characterized by an Ultra-Dense Cortical Graph, Maintains Specificity by Distinct Connectivity Profiles

Răzvan Gămănuț,[1] Henry Kennedy,[1,2,7,*] Zoltán Toroczkai,[3] Mária Ercsey-Ravasz,[4,5] David C. Van Essen,[6] Kenneth Knoblauch,[1] and Andreas Burkhalter[6,*]

[1]Université Lyon, Université Claude Bernard Lyon 1, INSERM, Stem Cell and Brain Research Institute U1208, 69500 Bron, France
[2]Institute of Neuroscience, State Key Laboratory of Neuroscience, Chinese Academy of Sciences (CAS) Key Laboratory of Primate Neurobiology, CAS, Shanghai 200031, China
[3]Interdisciplinary Center for Network Science and Applications, Department of Physics, University of Notre Dame, Notre Dame, IN 46556, USA
[4]Faculty of Physics, Babeş-Bolyai University, 400084 Cluj-Napoca, Romania
[5]Romanian Institute of Science and Technology, 400487 Cluj-Napoca, Romania
[6]Department of Neuroscience, Washington University School of Medicine, St. Louis, MO 63110-1093, USA
[7]Lead Contact
*Correspondence: henry.kennedy@inserm.fr (H.K.), burkhala@wustl.edu (A.B.)
https://doi.org/10.1016/j.neuron.2017.12.037

## SUMMARY

**The inter-areal wiring pattern of the mouse cerebral cortex was analyzed in relation to a refined parcellation of cortical areas. Twenty-seven retrograde tracer injections were made in 19 areas of a 47-area parcellation of the mouse neocortex. Flat mounts of the cortex and multiple histological markers enabled detailed counts of labeled neurons in individual areas. The observed log-normal distribution of connection weights to each cortical area spans 5 orders of magnitude and reveals a distinct connectivity profile for each area, analogous to that observed in macaques. The cortical network has a density of 97%, considerably higher than the 66% density reported in macaques. A weighted graph analysis reveals a similar global efficiency but weaker spatial clustering compared with that reported in macaques. The consistency, precision of the connectivity profile, density, and weighted graph analysis of the present data differ significantly from those obtained in earlier studies in the mouse.**

## INTRODUCTION

The concept of the cortical area is rooted in the notion of localization of function in the cortex, where individual areas are posited to have a distinct architecture, connectivity, function, and/or topographic organization (Felleman and Van Essen, 1991; Van Essen, 2003). The mouse is increasingly used as a model system for investigating the cortex, where complex sensory (Ferezou et al., 2007), motor (Li et al., 2016), and cognitive (Carandini and Churchland, 2013; Kim et al., 2016; Manita et al., 2015) functions have been shown to depend on interactions among cortical areas via inter-areal connections as well as on dynamic control involving higher-order thalamic nuclei (Mease et al., 2016; Sherman, 2016). The highly interactive nature of cortical processing motivates efforts to investigate the statistical properties of inter-areal networks (Wang and Kennedy, 2016) and the development of large-scale models of the cortex that may provide insights into brain function in health and disease (Bullmore and Sporns, 2012).

Early evidence for distributed hierarchical processing within the cortex (Felleman and Van Essen, 1991) drew on collated tract-tracing data from numerous studies using diverse methods of generally low sensitivity. This limited the reliability of inferences about statistical features of large-scale cortical networks (Kennedy et al., 2013) and, notably, led to underestimating the density of the cortical graph (i.e., the fraction of connections that can exist that do exist). This, in turn, leads to a failure to appropriately constrain the range of plausible models of cortical networks (Markov et al., 2013b). These considerations motivate the development and use of sensitive tract-tracing methods along with accurate areal parcellation (Bassett and Bullmore, 2016). The high density and wide range of connection strengths of the cortical graph (Markov et al., 2011, 2014a) point to the importance of quantifying the *weights* of the connections linking different cortical areas (Ercsey-Ravasz et al., 2013; Oh et al., 2014; Song et al., 2014; Ypma and Bullmore, 2016).

Recent quantitative retrograde tracer studies in the macaque (Markov et al., 2011, 2014a) demonstrated that, compared with previous studies, there were many more inputs to each cortical area, a wider 5-order magnitude range of connection strengths to each area, and a much narrower range of variability in the strength of individual pathways tested with repeat injections. These findings support the concept of each area having a distinctive fingerprint or connectivity profile defining its functional specificity (Bressler and Menon, 2010; Markov et al., 2011; Passingham et al., 2002); they contrast with earlier reports suggesting that connection weights in cortical pathways are

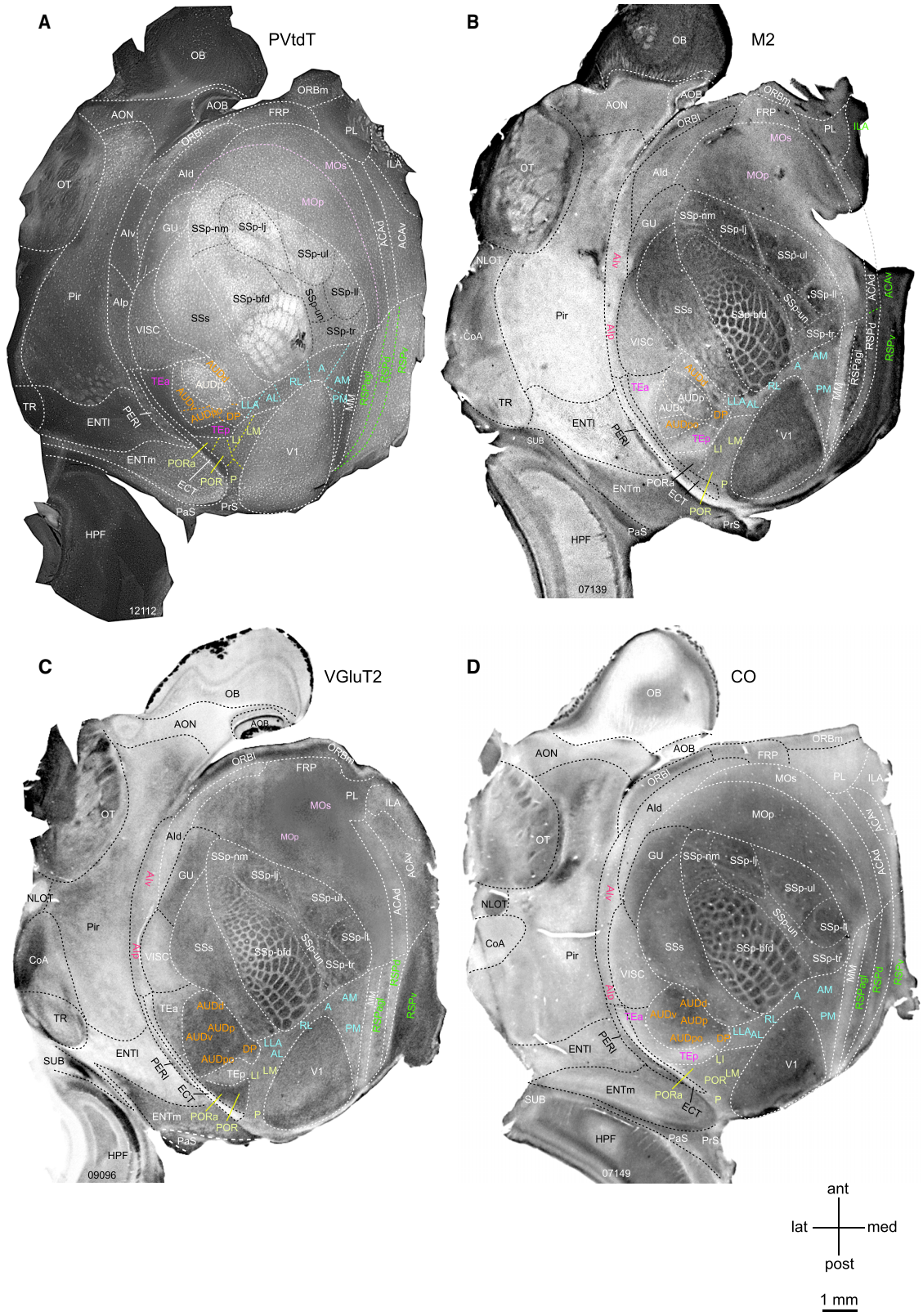


*(legend on next page)*

highly variable across individuals (MacNeil et al., 1997; Musil and Olson, 1988a, 1988b; Olson and Musil, 1992; Scannell et al., 2000). Hence, it is important that the mouse database be investigated for its statistical variability of connection weights to estimate the validity of the connectivity profiles.

The weight-distance relations observed in macaque cortical connectivity data lead to a one-parameter predictive model that captures multiple features of the cortical network, including its spatial embedding, wire minimization, frequency distribution of motifs, global and local efficiencies, and a core-periphery architecture (Ercsey-Ravasz et al., 2013). Spatial embedding constrains numerous geometrical features in a similar fashion in the mouse as well as the macaque cortex (Horvát et al., 2016).

A recent systematic connectivity study obtained brain-wide weighted data (Oh et al., 2014) using anterograde tracer injections on a fixed grid of injection sites. Because most of the reported injection sites (>70%) spanned multiple areas, connectivity at the level of individual areas was inferred using a computational model involving several theoretical assumptions. Their probabilistic model of connectivity yielded an estimated density for the inter-areal cortical graph of 35%–53%, much lower than the 66% reported for the macaque cortical graph (Markov et al., 2014a). The lower density reported in the mouse and also in the rat (Bota et al., 2015) is surprising, given that one might anticipate increased graph density with decreasing brain size (Horvát et al., 2016; Ringo, 1991). Furthermore, an earlier tracer study of the mouse *visual* cortex (Wang et al., 2012) reported a considerably higher subgraph density (99%) than the 77% reported for visual areas by Oh et al. (2014). These findings suggest that the computational procedure used in the Oh et al. (2014) study to infer the connectivity of single areas from injections involving multiple areas might have resulted in significant numbers of false negatives. A re-analysis of the Oh et al. (2014) dataset estimated a whole-cortex graph density of 73% (Ypma and Bullmore, 2016). Hence, in the present study, we focused on an empirical approach that is deterministic because it depends on direct anatomical observations.

Here we investigate mouse cortico-cortical connectivity and address two key issues: the density of the mouse cortical graph and the consistency of connectivity profiles across individuals. We minimized experimental variability by targeting injections of a retrograde tracer in post hoc-identified areas rather than a fixed grid of anterograde injections (Oh et al., 2014). Our choice of retrograde tracer provides several advantages for quantifying connection strengths (see Suitability of DY Tracing in the STAR Methods for a detailed discussion). We coupled retrograde tracing with flat-mounting the cortex, which is particularly advantageous when combined with multiple histological stains used for cortical parcellation (Qi and Kaas, 2004; Sincich et al., 2003; Wang and Burkhalter, 2007; Wang et al., 2011, 2012). Our experimental approach allows positive identification of both injected cortical areas and of 41 areas and 7 sub-areas where the retrogradely labeled neurons are located.

Our results show that the mouse cortex is ultra-dense, with a graph density of 97%, significantly higher than the probabilistically based range of 35%–73% (Oh et al., 2014; Ypma and Bullmore, 2016). The high density of the mouse cortical graph suggests that the activity pattern of a given area is interrelated, via its connectivity profile, to a widespread pattern of influences across the cortex. It seems implausible that smaller brains would be associated with greater variability of connection weights (as reported in Oh et al., 2014) because this, in conjunction with a high graph density, would entail lower specificity of the structure and function of the mouse cortical network compared with the macaque. Our analysis of the present retrograde labeling revealed variability of connectivity and connectivity profiles in the mouse comparable with those observed in the macaque (Markov et al., 2014a). Likewise, our deterministic approach leads to a weight-distance relationship that is quantitatively similar in mouse and macaque (Horvát et al., 2016), in contrast to the modeled data from the Oh et al. (2014) study. Our results demonstrate that the densely interconnected network of the mouse cortex contains highly selective area-to-area connectivity profiles that, in primates, underlie distributed hierarchical cortical processing (Markov et al., 2011).

## RESULTS

### High-Resolution Cortical Parcellation

The spatial precision of the alignment of diamidino yellow (DY) labeling with the areal map is a critical experimental issue, given the small size of the mouse cortex. PVtdT mice allowed parcellation of the cortex into 25 parcels, excluding the entorhinal, hippocampal, and piriform cortex (Figure 1A), and provided

**Figure 1. Expression of M2, VGluT2, and CO with Respect to PVtdT in Layer 3/4 of the Flat-Mounted Left Mouse Cerebral Cortex**

(A) Tangential section showing tdTomato (tdT) fluorescence in parvalbumin (PV)-containing interneurons (bright white labeling). Parcels outlined by white dashed lines and labeled by black and white letters were positively identified by PVtdT expression. Black dashed lines indicate subdivisions within the primary somatosensory (SSp) cortex, representing different body parts. Colored letters denote known areas contained within distinct compound parcels (orange, yellow, blue, green, pink, and purple) in which PVtdT expression exhibits similar intensity and reveals no detectable subdivisions. Colored dashed lines indicate presumptive borders between these areas.

(B) Bright-field image of a tangential section stained with an antibody against the M2 muscarinic acetylcholine receptor (dark staining). Areas outlined with white and black dashed lines and denoted with white and black letters were positively identified as distinct parcels. Areas denoted in orange, yellow, blue, green, pink, red, and purple letters indicate known areas contained within distinct but uniformly M2-labeled parcels.

(C) Bright-field image of a tangential section stained with an antibody against VGluT2 (dark staining). Areas outlined with white and black dashed lines and denoted in white and black letters were positively identified as distinct parcels. Areas denoted in orange, yellow, blue, green, pink, and red letters indicate known areas contained within distinct but uniformly VGluT2-labeled parcels.

(D) Bright-field image of a tangential section reacted for cytochrome oxidase (CO) activity (dark staining). Areas outlined with white and black dashed lines and denoted in white and black letters were positively identified as distinct parcels. Areas denoted in orange, yellow, blue, green, red, and purple letters indicate known areas contained within distinct but uniformly CO-labeled parcels.

See also Figures S1 and S5.

reliable landmarks for aligning matching/complementary expression patterns of M2, VGluT2, cytochrome oxidase (CO) (Figures 1, S1C, and S1D), and visuotopically mapped borders (Wang and Burkhalter, 2007). In each brain, this procedure allowed positive identification of 115 of the 133 borders (86.5%); the remaining borders were inferred from the known patterns of CO, M2, and VGlutT2 (Figure S1B). Importantly, because the brain map is created for each tangentially sectioned individual brain, it avoids assigning labeled cells to a standard template and obviates aligning large numbers of adjacent sections. Our approach largely takes into account the individual differences in parcellation across subjects (Krubitzer and Seelke, 2012) and significantly differs from that employed in two recent studies (Oh et al., 2014; Zingg et al., 2014) that mapped corticocortical projections onto a standard Allen Reference Atlas (ARA; Dong, 2008), generated by averaging variations of background fluorescence across hundreds of cortices. This common coordinate framework (CCF, Allen Institute for Brain Science, http://brain-map.org) has become a widely used parcellation of the mouse cerebral cortex (Figure S1A).

Within the 25 parcels, additional areas were identified by comparing PVtdT with the patterns of M2, VGluT2, and CO expression (Figures S1C–S1F). These included the postrhinal area (POR), postrhinal anterior (PORa) (previously referred to as 36p; Wang et al., 2011), auditory cortex ventral area (AUDv), auditory cortex posterior area (AUDpo), dorsal posterior area (DP), motor cortex primary area (MOp), motor cortex secondary area (MOs), retrosplenial area agranular part (RSPagl), retrosplenial area dorsal part (RSPd), retrosplenial area ventral part (RSPv), temporal area anterior part (TEa), and temporal area posterior part (TEp). The borders of the visuotopically mapped areas (posterior area [P], laterointermediate area [LI], laterolateral anterior area [LLA], rostrolateral area [RL], anterior area [A], anteromedial area [AM], and posteromedial area [PM]; Garrett et al., 2014; Wang and Burkhalter, 2007; Zhuang et al., 2017) were only partially outlined by any of the molecular markers. Here the missing borders could be filled in by registering PVtdT maps to instructions based on the stereotypical size, shape, and relative position of areas derived by previous visuotopic mapping (Wang and Burkhalter, 2007). Where this procedure differs from template matching is that areal boundaries are derived from the PVdtT map of each individual case. The grand total was 41 areas, of which the primary somatosensory cortex (SSp) was subdivided into 7 subareas (Figure S1B). The variance of areal border assignments was estimated to be <150 μm (for details, see Parcellation of the Cortex in the STAR Methods).

### *Retrograde Tracing with DY*

For details about DY, see Suitability of DY Tracing in the STAR Methods. Representative examples of the DY labeling at low power are shown in Figures 2A–2F (note that cell counts were acquired using higher magnification). The area V1 (primary visual area) injection shown in Figures 2A–2C was confined to the lower peripheral visual field representation near the tip of V1 (Marshel et al., 2011). As expected from previous axonal tracing and topographic mapping experiments (Garrett et al., 2014; Marshel et al., 2011; Wang et al., 2007), retrogradely DY-labeled neurons were clustered at the junction of the lateromedial area (LM), anterolateral area (AL), LI, and LLA. Additional clusters of labeled neurons were found at retinotopically corresponding locations within RL, A, AM, PM, mediomedial area (MM), P, POR, and PORa. In the temporal cortex, DY labeling was contained in most areas of the auditory cortex (auditory cortex primary area [AUDp], AUDpo, AUDd, and DP) and the ventral portion of the posterior temporal area (TEp). On the medial wall, labeled neurons were clustered in dorsal retrosplenial cortex (RSPd), the secondary motor cortex (MOs), the dorsal and ventral anterior cingulate areas (ACAd and ACAv, respectively,) and in the prelimbic (PL) and infralimbic (ILA) cortex. At the rostral end of the cortex, labeling in the orbitofrontal cortex was confined to the orbitofrontal area lateral part (ORBl). A complete map of neurons projecting to V1 is shown in Figure S2. The densest inputs originate from the occipital, temporal, parahippocampal, retrosplenial, cingulate, orbitofrontal, and prefrontal cortex, whereas inputs from the parietal somatosensory, gustatory, visceral, and insular cortex are sparse or absent.

### *Statistical Consideration of Overdispersion*

Variability in the retrograde tracer data from the present study was modeled by analyzing the statistical properties of connections resulting from repeat injections of tracers across individuals. Scatterplots of the SD versus the mean (see Overdispersion in the STAR Methods) are shown in Figures 3A and 3B with the indicated dispersion values. Overall, the results indicate a negative binomial distribution with dispersion values of 6, which provides a reasonable estimate of the expected variability for neural counts obtained with retrograde tracing data in the mouse. The $\theta$ estimate of 6.1 for V1 and LM is somewhat smaller than that obtained in the macaque, 7.9 (Markov et al., 2011), suggesting marginally greater levels of overdispersion across animals in the mouse datasets. These findings demonstrate that overdispersion is a systematic phenomenon of neural retrograde count data in both the macaque and mouse. Thus, overdispersion needs to be considered in the statistical evaluation of such data because ignoring it would lead to anti-conservative estimates of the probabilities of significant differences in connection strengths; i.e., erroneously assigning significance to small differences.

Repeat injections make it possible to examine variability in the raw data of Oh et al. (2014) (Figures 3C and 3D). Although not based directly on counts, we applied the same framework to examine the variability in relation to the mean. In contrast to the retrograde tracer data, the anterograde data of Oh et al. (2014) show a dispersion of 1.6 for the somatosensory barrel field and 2.3 for area V1 and, therefore, in both cases indicate a more overdispersed dataset compared with the retrograde tracing data in the present study; the higher incidence in overdispersion in the anterograde data may be related to the difficulties in estimating projection strength from measurements of fluorescence intensity (see Effect of Template Matching on the Weight Distribution of Connections).

## Log-Normal Distribution of Weights

An intriguing aspect of cortical organization is that many physiological and anatomical features are distributed according to a log-normal distribution (Buzsáki and Mizuseki, 2014). This is a skewed, heavy-tailed distribution typically characterized by

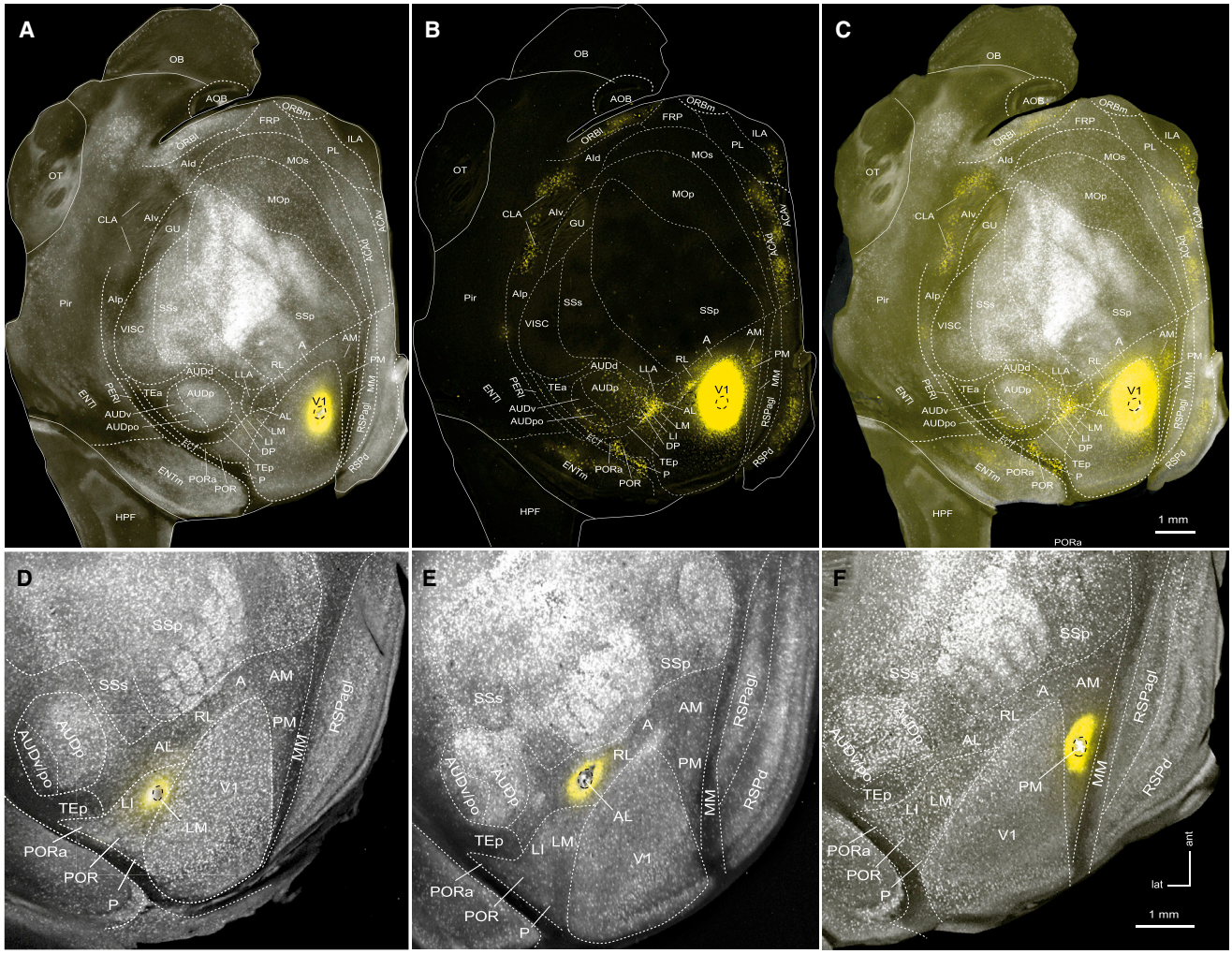


**Figure 2. Retrograde DY Labeling in PVtdT Mice**

(A) Tangential section (slightly tilted to the lateral side away from the tangential plane) through layers 3–5 of the flat-mounted cortex showing the distribution of PVtdT-expressing neurons (false-colored white). Parcel boundaries were assigned based on PVtdT expression densities. The false-colored yellow spot marks the DY injection site. Black dashed outlines indicate the border of the crystalline DY deposit, which is confined to the lower peripheral visual field representation of V1. Note that the injection site appears larger because of overexposure of the fluorescence image to visualize the labeled neurons.

(B) Same section as in (A), showing the distribution of retrogradely DY-labeled neurons (false-colored yellow dots). Note that, because of the long exposure time required to reveal DY-labeled neurons at low magnification, the injection appears larger than the site outlined (black dashed outlines) in (A). Importantly, DY-labeled neurons are tightly clustered at sites that match the topographic location of the injection site (Garrett et al., 2014; Marshel et al., 2011; Wang and Burkhalter, 2007).

(C) Overlay of images shown in (A) and (B).

(D–F) Tangential sections through layer 4 of the posterior half of the cortex in PVtdT-expressing mice, showing DY deposits (outlined by dashed black lines) in areas LM (D), AL (E), and PM (F). Although, under fluorescence illumination, the injection sites appear larger than the DY deposit, it is important to note that they are confined to individual areas.

See also Figures S2 and S7.

relatively few very strong and very weak values with many intermediate ones. A log-normal distribution was first reported for synaptic weights (Song et al., 2005) and subsequently as a characteristic of the distribution of input strengths to a cortical area in the macaque (Markov et al., 2011) and mouse (Oh et al., 2014; Wang et al., 2012).

Figures 3E and 3F show that, for areas LM and V1, the areas analyzed in Figures 3A and 3B, the ordered means of log (FLNe [extrinsic fraction of labeled neurons]; Markov et al., 2014a) values follow log-normal distributions. The range of values spans 4 to 5 orders of magnitude. The fitted curves (solid lines) do not fall outside of the expected variability, represented by the gray envelopes, indicating that the differences from the log-normal prediction are not significant (see Accordance with the Negative Binomial Model in the STAR Methods).

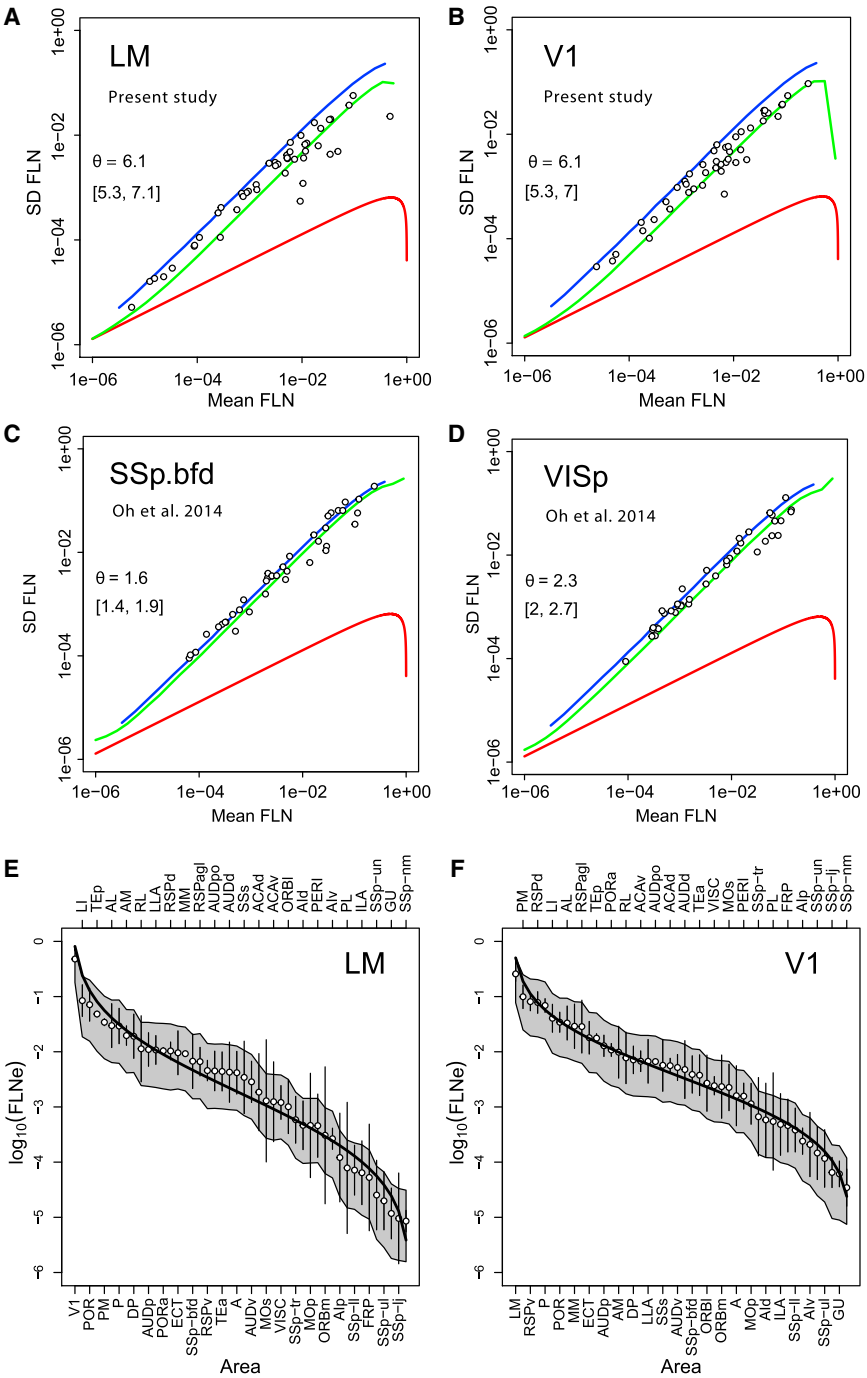


**Figure 3. Variance and Log-Normal Distribution of FLNe**

(A–D) Repeat injection SD as a function of the mean. θ, dispersion parameter; red curves, Poisson distribution; blue, geometrical distribution; green, negative binomial; brackets, 95% confidence interval.

(A and B) Retrograde DY tracer injections of (A) LM (n = 3) and (B) V1 (n = 4) (present study) of DY-labeled neurons.

(C and D) Anterogradely labeled projections described by Oh et al. (2014) after injections of a viral tracer into the mouse (C) somatosensory barrel cortex (SSp-bfd) (n = 5) and (D) primary visual cortex (VISp) (n = 8). Note the difference in $\theta$ values for (A) and (B) versus (C) and (D). To have the same normalization as in (A) and (B), for each injection, we divided the strengths of cortico-cortical projections by the sum of cortico-cortical projections from the injection.

(E and F) Log-normal distribution of retrograde tracing data in the present study, observed means (white dots) ordered by magnitude, and SEM (error bars) of logarithms of the FLNe for the cortical areas projecting to the injected area. (E) LM (n = 3), (F) V1 (n = 4). Black curves indicate the expected log-normal distribution for an ordered set of projections of size n, equal to the number of source areas. The gray envelopes around each curve indicate the 95% confidence intervals obtained by simulating 10,000 sets of count experiments drawn from a negative binomial distribution, with means of counts and dispersion parameter as the data.

## Variability of Deterministic Connectivity Maps in Mouse and Monkey and the Consistency of Weak Connections

The repeatability of connections to a given area across individuals makes it possible to evaluate the variability in terms of consistency of individual pathways. By consistency, we refer specifically to whether a connection is systematically present across injections (see Variability and Consistency in the STAR Methods).

Figures 4A–4C show violin plots of means of projections for repeat injections and explores the variability of the set of inputs to a given cortical area across individuals. In this figure, connected areas that are found for all repeat injections in an area are shown in gray and those that are absent from a given injection in red. The present study shows low variability across injections. Medium to strongly connected areas were found systematically after each injection (Figure 4A). Similar findings were obtained in the macaque (Figure 4B). The macaque data (Markov et al., 2014a) differed from the present observations in the mouse in that similar levels of inconsistent projections were found in ten of the 13 repeats compared with only three of the 13 in the mouse (Figure 4B). The higher variability in the macaque could be related to the partial sampling in the macaque study. The relatively low level of variability in the retrograde tracer studies of mouse and macaque differs from the high variability observed in the raw data in the Oh et al. (2014) anterograde data, in which inconsistent projections were found across nearly all injections and at much larger weight values (Figure 4C).

In Figure 4D, of the 598 possible connections from repeat injections, 581 (97.2%) were present and 17 (2.81%) were absent.

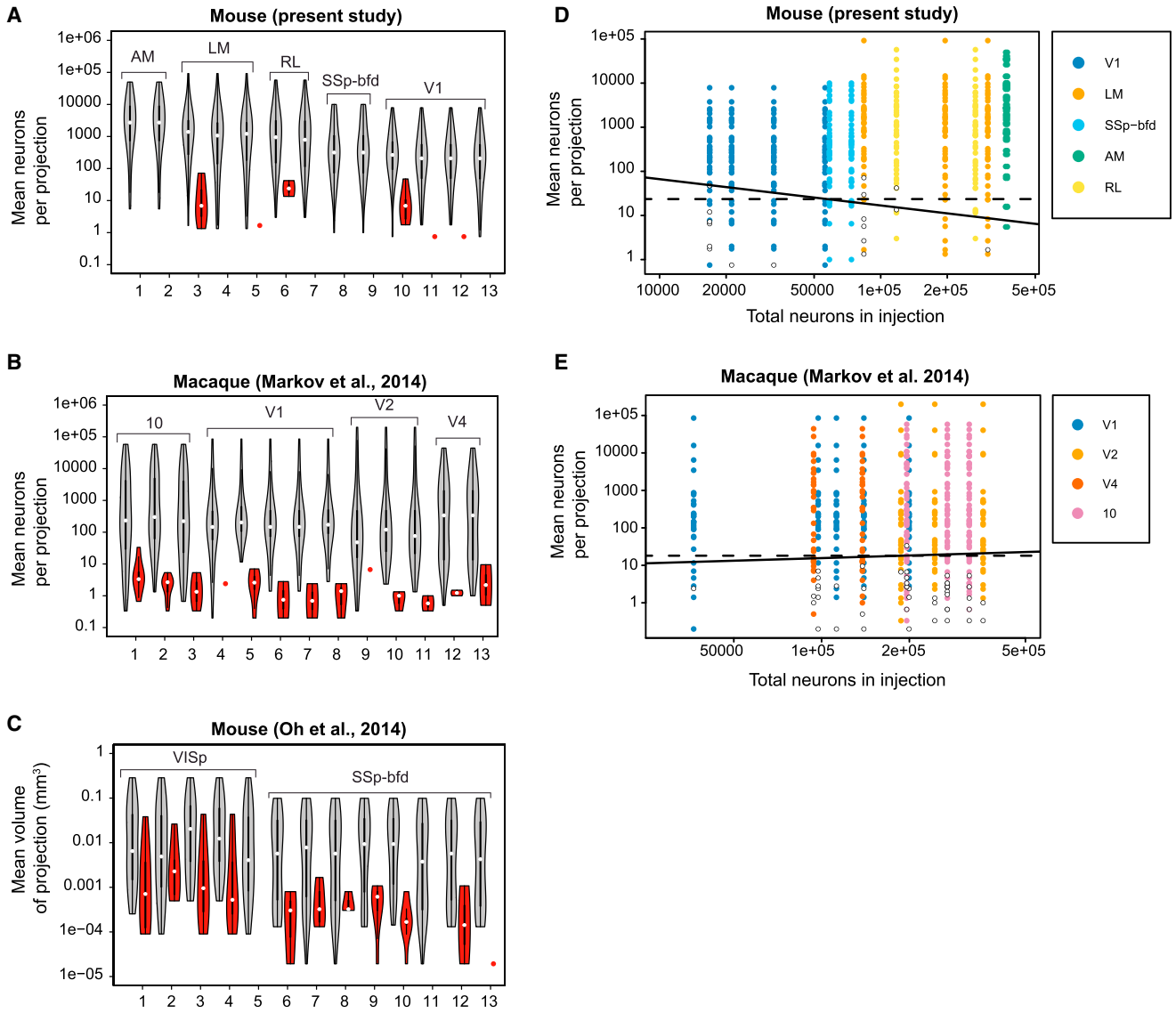


**Figure 4. Consistency in Mouse and Macaque as a Function of Mean Weight and Size of Injection for Repeat Injections across Individuals**

(A–C) Violin plots of means of projections consistent across repetitions (gray) and of inconsistent projections (red).

(A) Mouse retrograde tracing data from the present study, representing repeat injections in areas AM, LM, RL, SSp-bfd, and V1.

(B) Macaque retrograde tracing data from repeat injections in areas V1, V2, V4, and 10 (Markov et al., 2014a).

(C) Mouse anterograde raw data, where repeat injections were restricted to single areas (VISp and SSp-bfd) (Oh et al., 2014). To have non-normalized data as in (A) and (B), we multiplied each strength of cortico-cortical connections with the volume of the respective injection taken from the supplemental data of Oh et al. (2014).

(D and E) Colored dots represent projections that are present; white dots indicate absent projections. On the vertical axis are represented the mean numbers of neurons per projection; on the horizontal axis is shown injection size in terms of total number of labeled neurons per injection. The solid lines correspond to a linear classifier from a logistic regression, with the variables of both axes used as features for a probability of the presence of the projection at 95%. The dashed lines correspond to a similar criterion for which only the ordinate variable was used as a classification feature.

(D) Repeat injections of the retrograde tracer DY in mouse areas V1 (n = 4), LM (3), RL (2), SSp-bfd (2), and AM (2).

(E) Repeats in macaque areas 10 (3), V1 (5), V2 (3), and V4 (2).

Absent connections are concentrated in the lower half of the diagram, where low mean numbers of neurons per projection are found. The continuous line in Figure 4D indicates the estimated linear classifier for which the probability of a connection being present is 0.95 for this model. Its negative slope suggests a dependence of connectivity on both features so that small injections would lead to higher probabilities of absence at high mean connection strengths. However, only the mean of projection was found to contribute significantly to the linear classifier (log(Mean), $z = 5.57$, $p = 2.56 \times 10^{-8}$; log(Total), $z = 1.7$, $p = 9.6 \times 10^{-2}$),

demonstrating no support for this hypothesis. The 95% classifier based only on the log(Mean) is indicated by the dashed line and corresponds to a value of 24 neurons. This indicates that projections containing more than 24 neurons on average will be highly consistently identified (but not always perfectly) across individuals.

In Figure 4E, we performed a similar analysis of the macaque data reported by Markov et al. (2014a) from repeat injections in areas V1, V2, V4, and 10. The solid and dashed lines correspond to the same models as in Figure 4D but fitted to the macaque data. Again, the influence of the total size of the injection was not found to contribute significantly to the classifier. The dashed line corresponds to a mean of 18 neurons, slightly lower than the value found for the mouse data and close to the value of 10 estimated more informally by Markov et al. (2014a).

Verification of the model of data variability, estimation of dispersion and consistency, and the generality of the log-normal distribution of weights and consistency justified the use of a single cortical injection of retrograde tracer in the macaque to characterize the projection profile of an area (Markov et al., 2014a). The present results show that this also holds for the retrograde labeling of cortical pathways in the mouse.

## The Mouse Cortical Connectome Exhibits Distinct Connectivity Profiles

Armed with a description of the distribution of the data, we tested whether there are signatures in the sets of projections to each area, as is the case in the macaque (Markov et al., 2011). Alternatively, every individual might present its own sets of connections and weights. Specifically, we examined each set of multiply injected areas to determine the minimum number of factors accounting for the systematic effects on the data (see Evaluating Akaike Information Criterion in the STAR Methods).

For areas LM and V1, the model without interaction between the explanatory variables AREA and BRAIN led to a decrease in Akaike's information criterion (AIC) (LM, difference in AIC [dAIC] = 23.8; V1, dAIC = 71.4). Thus, for both areas, this model yields a better or equivalent balance between complexity and goodness of fit than the more complex model. The optimal models were those for which individual differences appeared as unsystematic variability; i.e., without an interaction between the areas and the individual animals. The presence of such an interaction would have signified the presence of individual differences in connectivity profiles beyond the variability among animals. Its absence implies that quantitative connectivity profiles do not differ sufficiently across cases and, therefore, that a robust signature (connectivity profile) exists for each area.

Is it possible to observe a connectivity profile when there is overdispersion? In the hypothetical case of a Poisson distribution (Figure 5A; see Overdispersion and Connectivity Profiles in the STAR Methods), the tight distribution of points about the ordered log-normal curve indicates that such Poisson data would show a clear example of a connectivity profile or signature, and an individual injection would be likely to closely reflect the average behavior indicated by the red curve. At the other extreme is the geometric distribution (Figure 5C), where the high variability (2–3 orders of magnitude range of variation for each projection) obscures the systematic trend of the expected curve (blue). As shown in simulations by Scannell et al. (2000), data distributed in this fashion would require an inordinate number of repeat injections to establish the average behavior of the curve with sufficient precision. Note that individual injections could follow any arbitrary path through the point cloud, so their value in establishing an areal profile would be of limited informative value. In this case, statistical analysis of a small number of injections would likely lead to the conclusion of individual differences in the profile for a single injection site; that is, the presence of a statistically significant interaction between area and brain injected. The simulated results from a negative binomial distribution (Figure 5B) with a dispersion parameter similar to that found in retrograde labeling in the macaque and mouse falls in between the Poisson and geometric distributions. However, with the variation of individual injections being only 1 order of magnitude, far less than the span of the ordered log-normal curve, single injections are much more representative of the average curve than for geometrically distributed data. As shown in our data, the variation among animals is not sufficient to reject the proposition that projection profiles from different animals are the same.

To illustrate the effects of a geometric distribution (Figure 5C) of the anterograde data and negative binomial distributions (Figure 5B) for the retrograde data on connectivity profiles, we show a boxplot analysis for area V1 for the present data (Figure 5E) and for the Oh et al. (2014) data (Figure 5F). This shows that the negative binomial distribution corresponds to a significantly more demarcated connectivity profile compared with the data with a geometric distribution in Figure 5F from Oh et al. (2014).

## Effect of Template Matching on the Weight Distribution of Connections

Comparison of raw connection strengths with those obtained from the computational model in Oh et al. (2014) allows appraisal of the modeling assumptions used in that study (see Processing Oh et al. (2014) Data in the STAR Methods). Figure 6A shows the agreement between the raw and the computed connections, with only 65% of them being true positives or true negatives, whereas 33% are false negatives (found in raw, but not in computed, connections) and 2% false positives (found in computed, but not in raw, connections). Moreover, the squared correlation between the true positives is modest, only 0.58. Comparison of the weight distribution of the raw and computed data gives further insight into how the computational algorithm of Oh et al. (2014) transforms the raw data (Figure 6B). Here the blue bars are the connections that result from the raw non-mixed injections and red bars the computed set of connections corresponding to the raw connections. The computed data equivalent to the 14 injected areas return 314 connections, significantly less than the 478 connections observed in the raw data. The 164 connections that are present in the raw data but are absent in the computed data (white bars), although predominantly weak, are nevertheless found throughout the full range of weights. Figure 6B, using a log scale for connection strength, suggests that the Oh et al. (2014) raw data do not follow the same log-normal distribution as the computed data.

In Figure S3, 19 of the 41 cortical areas in an adapted atlas from the present study correspond to areas listed in the Figure 6C legend in the atlas used by Oh et al. (2014), allowing some direct

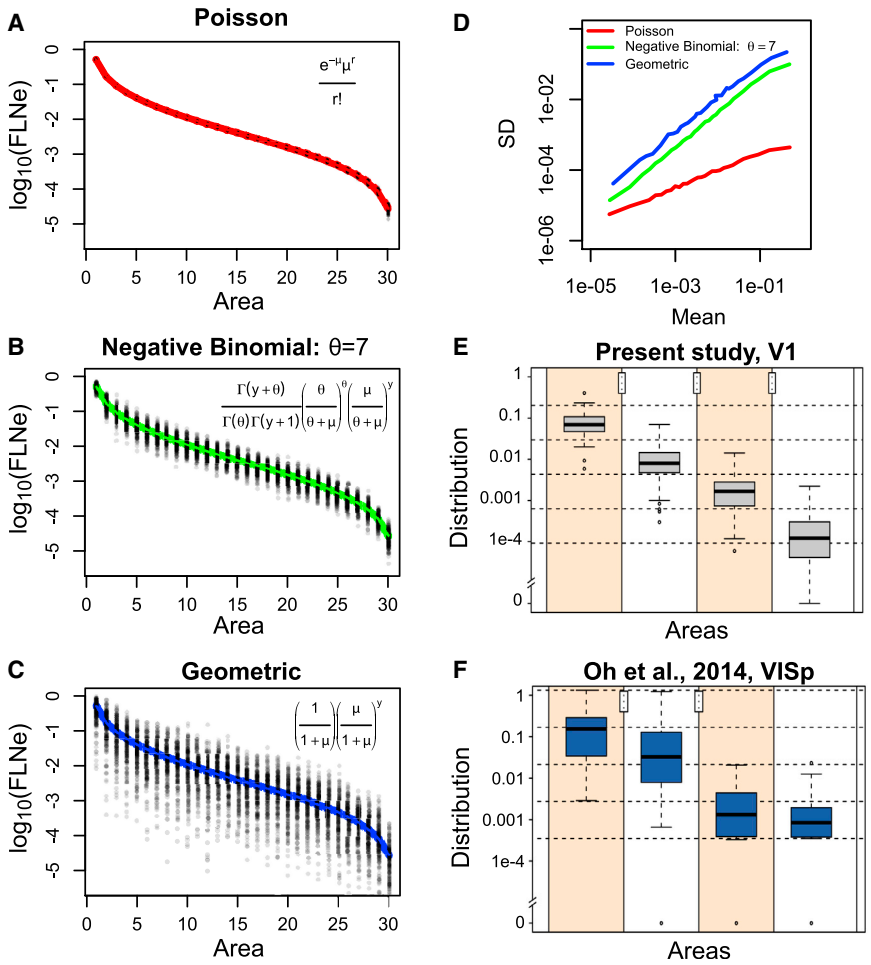


**Figure 5. Relations of Discrete Probability Distributions on Log-Normal FLNe Distribution Variabilities and Connectivity Profiles**

(A–C) The hypothetical results of 1,000 injections were simulated according to Poisson (A), negative binomial (dispersion parameter $\theta$ = 7) (B), and geometric distributions ($\theta$ = 1) (C).

(D) The SD is plotted as a function of the means calculated for the simulated injections from (A)–(C), with the colors indicating the distribution from which the calculations were made.

(E and F) Example of the effect of overdispersion on the reliability of projections in the present data (E) and in Oh et al. (2014) (F). In both plots, a single injection in V1 (VISp) was taken, and the areas were ordered according to their strengths. The difference between the log of the maximum and of the nonzero minimum was then divided into four intervals (delimited by dashed horizontal lines) and assigned the log of the FLNe to the corresponding intervals, forming four groups. Next, the strengths of the corresponding areas from the other repeats were used to obtain the boxplots. In all boxplots, the bold lines represent the medians and the boxes indicate the 25% and 75% quantiles. The whiskers extend to the most extreme data points, which are no more than 1.5 times the interquartile range from the boxes. The stars represent the significance levels attained of the p values of one-sided permutation tests for each pair of consecutive groups, with the null hypothesis that the mean of the group on the left is larger than the mean of the group on the right. Notice that the present data are all restricted to the initial intervals (within the limits of the dashed horizontal lines), whereas the data from Oh et al. (2014) in all but one case cross these limits.

comparison between the two studies. The present study found 142 connections in this set of common areas, which contrasts with the 87 connections computed for these areas by Oh et al. (2014). Figure 6C shows the set of connections shared by the two studies (the same source area and the same target area). This shows that the computed data from Oh et al. (2014) exhibit a log-normal distribution tightly restricted to the top three orders of magnitude compared with the broad log-normal distribution in the present study. Figure 6D provides a more direct comparison by contrasting only connections that are non-zero in both studies. They differ significantly in their weight range and, more importantly, show no correlation (inset, Figure 6D). These findings confirm that the algorithm used by Oh et al. (2014) to disentangle connections evidently led to significant transformations by reducing the number of connections and affecting their distribution of connection strengths. This is further supported by comparing those connections in the Oh et al. (2014) raw data with the 19 homologous connections in the present data (Figure 6E). Although the comparison is limited, this suggests that, compared with the computed data, the raw data in Oh et al. (2014) show an improved overlap in the weights and have a modest correlation with data from the present study (Figure 6E, inset). However, Figure 6F shows that the raw data of Oh et al. (2014) possess a narrower range of weights compared with the present study.

Elsewhere we have shown that the weight-distance relationship is a cardinal feature of the connectome in both mouse and monkey and that it accounts for statistical aspects of many network features, such as the motif distribution, similarity, and core-periphery (Ercsey-Ravasz et al., 2013; Horvát et al., 2016). In Figure 6G, we compare the decline of weight with distance in the computed and raw cortico-cortical connections from Oh et al. (2014). This shows only a very modest slope for the computed data; by contrast, the slope in the raw data is comparable with that found in the present study (Figure 6H). The slope of $-0.68$ mm$^{-1}$ obtained in the present study is similar to that obtained in Horvát et al. (2016). Finally, in the Oh et al. (2014) study, our analysis of their raw data from the 26 unmixed injections in 14 isocortical areas yields a density of 92%, which is consistent with the density of 97% observed from our injections (see Partial Coverage and Global Claims in the STAR Methods).

In anterograde tracing, it is challenging to distinguish between pre-terminal axons and boutons and to exclude labeled fibers of passage from the analysis. Further, there is an important difference in scale explored by the two tracers; anterograde is subcellular because it reveals individual boutons with hundreds to

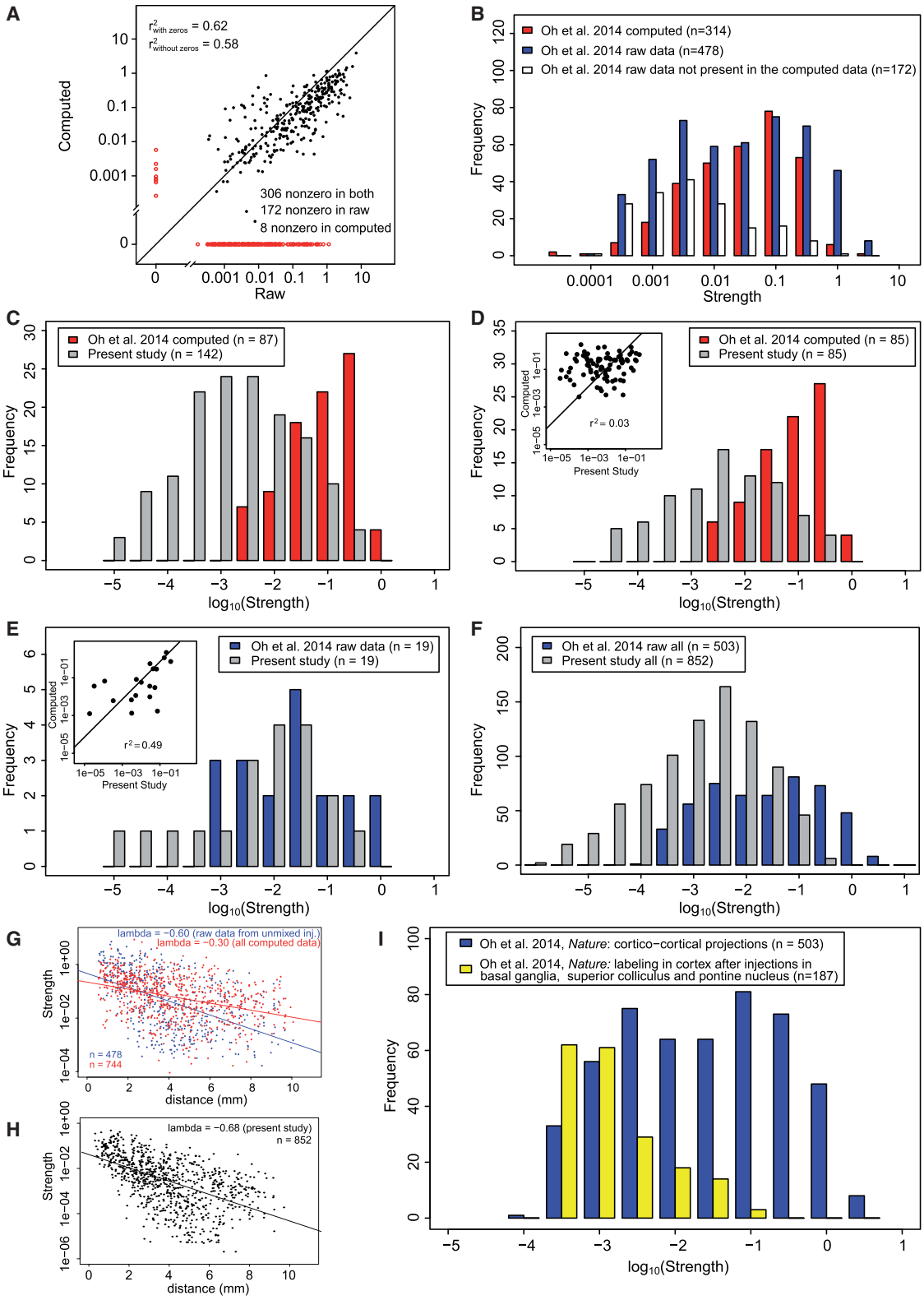


**Figure 6. Comparison of Data in the Present Study with Previous Findings**

The reported data in the present study show some similarity to the raw data in Oh et al. (2014), but not to the computed data of that study.

(A) Correlation between the raw and computed data in Oh et al. (2014), with zero values shown in red.

*(legend continued on next page)*

thousands per axon (Binzegger et al., 2004). In contrast, retrograde tracing is at the single-cell level. These differences are compounded by the challenge of distinguishing boutons from interbouton axons when quantifying projection strength by measuring optical density (Wang et al., 2012), a difficulty that may contribute to the greater overdispersion in the anterograde data compared with the retrograde data (Figure 3). Further, anterograde tracers occasionally label neurons retrogradely and with them their collaterals both in the injected area and other areas to which the collaterals project (Reiner et al., 2000). Estimates of terminal densities from anterograde tracers using optical density measurements where axons of passage can introduce a significant bias may be less accurate than counts of labeled neurons following retrograde tracers. Since the observations of LeVay and Sherk (1983), anterograde tracers have been shown to lead to retrograde labeling, and this includes the viral tracers used in the Oh et al. (2014) study (Wang et al., 2014). This can lead to labeling of local collaterals of the retrogradely labeled cells and could explain the secondary anterograde labeling observed in the Oh et al. (2014) study, in which anterograde injections in the pontine nucleus and superior colliculus led to levels of labeling in the cortex comparable with those reported for cortico-cortical projections (Figure 6I; Table S1). However, for measuring projection weights, anterograde and retrograde techniques are, in principle, complementary: retrograde labeling for revealing the diversity of source neurons and anterograde for informing about target specificity.

### The Ultra-High Density of the Cortical Graph

Figures 7A and 7B show the weighted connectivity of 19 × 47 and 19 × 19 matrices, in which the color of each entry represents the $\log_{10}$ (FLNe) value for that pathway. Each column provides the FLNe profile of inputs observed for a given area and each row its outputs. The rows and columns were ordered to maximize the overall similarity between neighbors. Source areas of the occipital, posterior temporal, and retrosplenial cortex are concentrated in the lower third of the matrix. Somatosensory, gustatory, visceral, insular, orbitofrontal, and prefrontal source areas are clustered in the upper third. Motor, cingulate, auditory, and parahippocampal source areas are mainly in the middle portion. Much to our surprise, we found connections between nearly all injected areas. Figures 7A and 7B show that the connection weights vary over 5 orders of magnitude, revealing two dissimilar but highly interconnected subnetworks. One exhibited strong connections between visual areas, strong inputs to the occipital cortex from the posterior parietal, auditory, and retrosplenial cortex, and moderate inputs from the somatosensory, motor, and orbital cortex, whereas projections from the visceral, gustatory, and prefrontal cortex were sparse. The other subnetwork (Figures 7A and 7B) exhibited strong inputs to the somatosensory cortex from the motor, visceral, gustatory, and insular areas; moderate input from the posterior parietal, and orbital cortex; and weak input from the retrosplenial and prefrontal areas. Inputs to both subnetworks from the cingulate parahippocampal and higher auditory cortex were similarly strong.

In the edge-complete 19 × 19 matrix (Figure 7B) (meaning that the connectivity status of all node pairs are known), most connections between pairs were reciprocal, except for 2% (8 of 342 were unidirectional), showing no detectable inputs from P, LM, AL, and RL to the gustatory area (GU) (Figure 7B) and from AL and PM to MOp. Note that, in Figure 7B, the distribution of colors is not perfectly symmetrical across the diagonal, indicating that the connection weights between pairs tended to be asymmetrical. For example, area MOp received only weak inputs from visual auditory and posterior parietal areas but projected back strongly to these areas. Overall, inputs from the gustatory, visceral, motor, somatosensory, and prefrontal cortex to visual and auditory areas were stronger than the ascending inputs from these sensory areas.

The $G_{19x19}$ graph has $M = 334$ (binary) directed links from the maximum possible of $N(N-1) = 342$, and, therefore, it is strongly interconnected, with a very high graph density of $\rho = 0.97$ (97%) (see Network Density in the STAR Methods). Because it is an edge-complete subgraph of the full interareal network (FIN), the density of $G_{19x19}$ is expected to be comparable with that of the FIN.

The in-degrees of the $G_{19x47}$ graph (i.e., the number of source areas projecting to each of the 19 target areas) range from 38 to 46 with a mean of $< k >_{in} = 44.8$ (Figure S4A); their distribution is asymmetrical and not concentrated around the mean but, instead, strikingly close to the maximum (Figure S4A, top right). To estimate the density of the FIN, the expected number of connections $M_{FIN} \sim < k >_{in} N_{FIN} = 2{,}107$ for the FIN ($G_{47x47}$) leads

(B) Distributions of the raw data and the corresponding connections in the computed data for the 14 areas that received unmixed injections in Oh et al. (2014). Red bars, computed data; blue bars, raw data; white bars, non-zero connections in the raw data but zero in the computed.
(C) Distribution of strengths of connections for areas that are homologous in Oh et al. (2014): computed data (red) and present study (gray). Source areas were as follows: anterior cingulate area dorsal part (ACAd), anterior cingulate area ventral part (ACAv), agranular insular area dorsal part (AId), agranular insular area posterior part (AIp), agranular insular area ventral part (AIv), ectorhinal area (ECT), GU, infralimbic area (ILA), MOp, MOs, ORBl, orbitofrontal area medial part (ORBm), ORBvl, perirhinal area (PERI), prelimbic area (PL), RSPd, RSPv, SSp-bfd, V1. Target areas were ACAd, GU, ILA, MOp, MOs, RSPd, SSp-bfd, and V1.
(D) Same as in (C) but considering only projections that are non-zero in both sets. Inset, correlation diagram.
(E) Distribution of strengths of connections for areas that are homologous and non-zero both in Oh et al. (2014), raw data (blue, the 14 areas that received unmixed injections), and the present study (gray). Inset, correlation diagram. Source areas were as follows: MOp, SSp-bfd, and V1. Target areas were as follows: ACAd, GU, ILA, MOp, MOs, RSPd, SSp-bfd, and V1.
(F) Distribution of connection strengths for the full dataset in the present study (gray bars) compared with raw data in Oh et al. (2014) shown in (B).
(G) Distribution of projection lengths in Oh et al. (2014), raw data (blue), and computed data (red).
(H) Distribution of projection lengths in the present study. Notice that the space constant is close to the one in the raw data in (G).
(I) Comparison of cortical labeling in Oh et al. (2014), following anterograde tracer injections in the superior colliculus, pontine nucleus, and basal ganglia with a label obtained following cortical injections.
See also Figure S3 and Table S1.

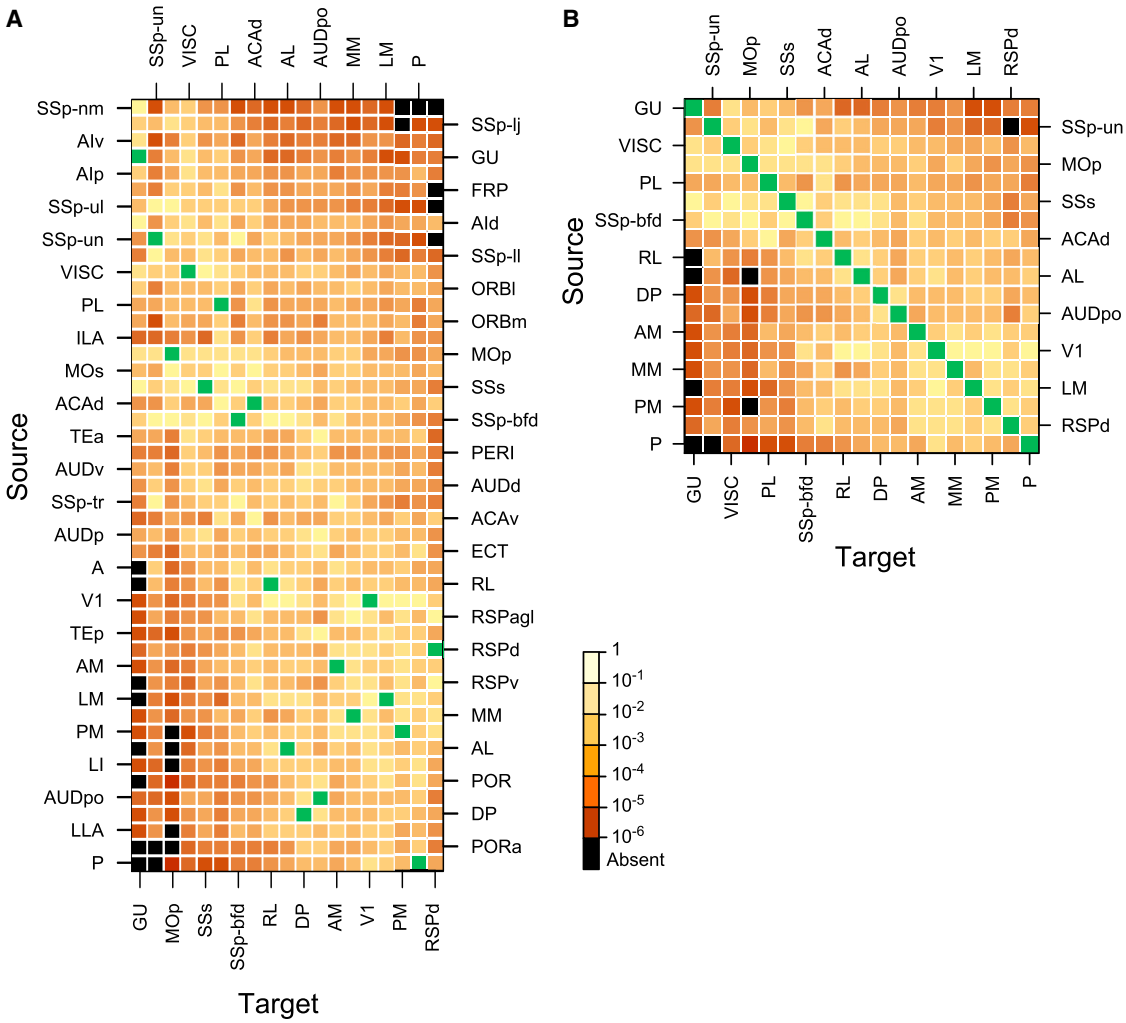


**Figure 7. Weighted Connectivity Matrix**

The strengths of the projections (FLNe) are color-coded: black, absent connections; green, intrinsic projections where FLN is not indicated. For multiple injections, FLNe indicates the arithmetic mean.

(A) Rows, one of the 47 source areas; columns, one of the 19 injected target areas. Note that the SSp-bfd and SSp-un subfields are listed as separate areas. The row and column ordering was determined by a clustering algorithm based on input and output profile similarity.

(B) A weighted connectivity matrix for the 19 × 19 subgraph.

See also Figures S4, S6, and S8 and Table S6.

to the prediction that $\rho_{FIN} = M_{FIN} / [N_{FIN} (N_{FIN} - 1)] \sim < k >_{in} / (N_{FIN} - 1) \sim 0.97$) (see Network Density in the STAR Methods).

A dominating set analysis (Markov et al., 2014a) shows that, for all sets of two target area combinations from the 19 target parcels (171 pairs), 92% of them dominate 100% of the 47 parcels (Table S2; see Network Density in the STAR Methods). Thirteen parcels of 19 (68%) are fully connected.

Because the present study sampled only 19 areas, we may ask whether it is legitimate to infer the high density of the full network from these data. To answer this question, we first examined the coverage of the injected areas across the cortex (Figure S5). This shows that injected areas are reasonably well distributed. Nevertheless, could we, by chance, have injected a subset of areas in the mouse that exhibit unusually high in-degrees? Our evidence indicates that this is not the case (see Partial Coverage and Global Claims in the STAR Methods); the necessary equivalence of in- and out-degrees coupled with graph theoretic analysis of the different datasets and parcellation schemes support the conclusion that the mouse cortical connectome is indeed ultra-dense.

## Communication Efficiency in the Weighted Cortical Network

Increasingly, the investigations of weighted networks are providing deeper insights into large-scale brain networks (Alstott et al., 2014; Bassett and Bullmore, 2016; Ercsey-Ravasz et al., 2013; Markov et al., 2013b; Muldoon et al., 2016; Song et al., 2014). Continued refinement of such approaches will be important for understanding the consequences of the ultra-high density network of the mouse brain relative to the sparser networks

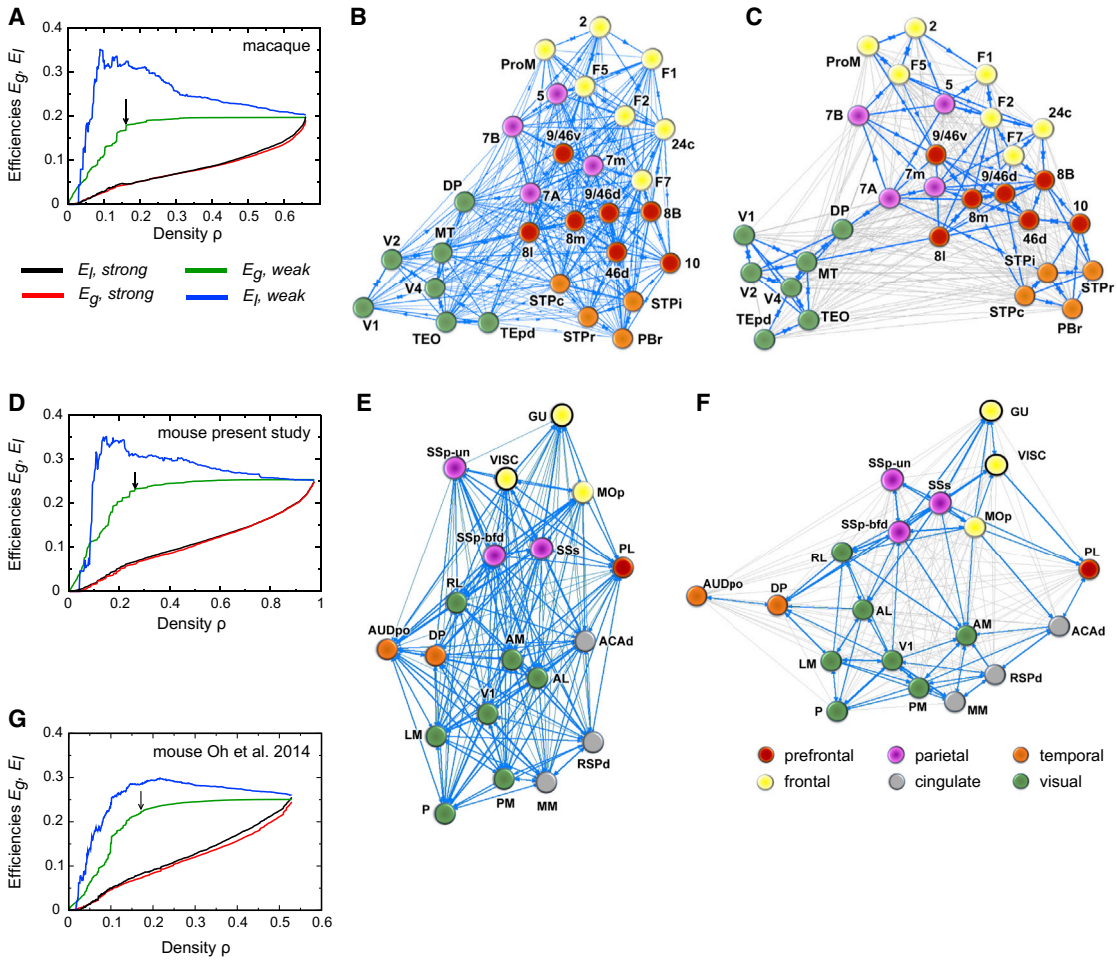


**Figure 8. Local and Global Communication Efficiency**

(A–C) Macaque data (taken from Ercsey-Ravasz et al., 2013).

(A) Effects of graph density, via sequentially deleting weak (blue, green) and strong (red, black) links, on global efficiency ($E_g$) and local efficiency ($E_l$). The black arrow shows where the graph exhibits onset of unreachability (16% density), indicating the high-efficiency backbone shown in (C).

(B) Weight-based layout, macaque full density (all 536 links). The Kamada-Kawai force-based algorithm for graph drawing reveals optimal layout, with edges representing springs proportional to the link weights.

(C) High-capacity backbone; blue edges are the 130 strongest connections (16% density) after weak link removal (thin gray edges), indicated by the black arrow in (A).

(D–F) Same analysis as in (A)–(C) but for present mouse data.

(D) The mouse graph exhibits onset of unreachability at 26% density.

(E) Weight-based layout, mouse full density (all 334 links).

(F) High-capacity backbone; blue edges are the 90 strongest connections (26% density) after weak link removal (thin gray edges), indicated by the black arrow in (B).

(G) Same analysis as in (A) but for mouse computed data from Oh et al. (2014).

of larger brains (see Network Communication Efficiency in the STAR Methods).

When sequentially removing from the macaque network the weakest (smallest FLNe) links, the global efficiency $E_g$ stays nearly constant (Figure 8A, green line) until more than 76% of the links are removed, indicating the existence of a high-bandwidth, global efficiency backbone embedded within the network. This ensures a stable, baseline, high-bandwidth average information transfer rate across the cortex, independent of the activity along the weak, long-range connections. The local efficiency $E_l$, however, shows a fast increase with the sequential removal of the weak links (Figure 8A, blue line). This happens because, as explained in Ercsey-Ravasz et al. (2013) and Markov et al. (2013b), pruning the interregional shortcuts makes the network more localized and modular and decreases interactions between the diverse functional modalities. As the weak links are removed, the local pathways between neighbors of a node through the rest of the network are mostly made of high-bandwidth (large FLNe) projections, resulting in higher conductance values. The picture that emerged from this analysis for the macaque was that the cortical network has a structure that is well adapted to high-volume local information processing via high-conductance local pathways and also to a stable, nearly constant efficiency level of global information processing. It also revealed the relationship

between network modularity and long-distance functional interactions, illustrated by the distribution of network communities that form when weak long-range links are present or absent (Figures 8B and 8C).

How does the mouse network compare with the macaque? Figures 8D–8F show the results of the same analysis for the mouse data. Interestingly, the overall behavior of transmission efficiency is similar between the two mammals, suggesting that these features are strongly constraining for the mammalian brain. Because $E_g$ and $E_l$ are both captured by the exponential distance rule (EDR) in the macaque (Ercsey-Ravasz et al., 2013) and because EDR holds in the mouse as well (Horvát et al., 2016), this reflects EDR as an organizational principle. In the mouse, as in the macaque, the areas also cluster into functional regions (compare Figure 8E with Figure 8B). Further, the high-bandwidth backbone (Figure 8F) presents stronger clustering than the full network (Figure 8E), just like in the macaque (compare Figure 8C with Figure 8B). However, there are significant differences between the two species. From a network point of view, the clusters in the macaque are stronger, with more high-bandwidth intra-cluster connections than high-bandwidth inter-cluster connections, especially for primary areas, whereas in the mouse the clusters are weaker, with significant inter-cluster high-bandwidth connections. Moreover, although there are no strong connections between primary areas in the macaque, those do appear in the mouse, notably with a projection from V1 to the SSp barrel field (SSp-bfd). When the same analysis is repeated on the Oh et al. (2014) data (Figure 8G), the local efficiency has a weaker increase relative to the global efficiency compared with the present mouse data (Figure 8D) and macaque data (Figure 8A). This presumably happens because of the inconsistencies discussed in the rest of the article.

## DISCUSSION

We find that mouse interareal connectivity is comparable with the macaque in showing relatively high consistency and well-defined connectivity profiles but differs in possessing a much higher graph density. Our findings, using a deterministic methodology, give significantly different results from the computational data reported by Oh et al. (2014), and we explored the effect of these differences via an analysis of the high-efficiency backbone. Finally, this weighted graph analysis reveals marked differences in the cortical connectomes of the mouse and macaque.

### Technical Considerations

PVtdT-expressing mice allowed accurate areal parcellation in each brain used for tracer injections, as reflected in the spatial map of labeled projection neurons shown in Figure S2. The utilization of quantitative retrograde tracing in these flat maps was an important part of our experimental design, aimed at minimizing inter-animal sampling errors. The experimental design of the present study made it possible to verify that the uptake zone of the injection site (see Suitability of DY Tracing in the STAR Methods) was entirely confined to the intended area for the 27 cases fully analyzed (of 102 injections). Modeling of FLNe variance in repeat injections across animals allowed exclusion of a geometric distribution in favor of a negative binomial distribution (Figure 3). Ranking FLNe values revealed log-normal distributions spanning 5 orders of magnitude with estimated 95% confidence intervals that satisfactorily contained the mean values (Figure 3). In addition, the consistency analysis of repeat injections showed that means in excess of twenty-four labeled neurons showed high consistency across injections (Figure 4). Finally, the dominating set analysis of the cortical subgraph studied here suggests that the full matrix may indeed have a density of 97% (Figure 7).

This density is considerably higher than the maximum 53% reported in the probabilistic mouse connectivity matrix (Oh et al., 2014) and in a meta-analysis of rat intracortical connections (Bota et al., 2015). High connection density might be caused by spillage of DY beyond the borders of areas or gray matter and/or uptake by fibers of passage and damaged axons (Keizer et al., 1983). Although such concerns are difficult to rule out entirely, examination of image stacks (Figure 2) revealed the location and 3D extent of the injection sites, allowing us to eliminate cases with spillage across areal and gray/white matter borders. Another potential concern involves labeling of area-to-area-projecting neurons via tracer uptake by inadvertently injured axons running through layers 5 and 6 (Coogan and Burkhalter, 1993). Control experiments (not reported here) indicate that injuring callosal fibers is necessary for retrograde DY labeling of interhemispheric projecting neurons, whereas application of DY to uninjured fibers of passage is ineffective. Thus, judged by the tight and topographically precise distribution of DY-labeled cells (Figures 2 and S2), we consider labeling via interareal deep-layer axons likely to be negligible.

Our experimental design involved implementing a procedure to parcellate the mouse cortex that was applicable in each experimental case and therefore avoided registration to a template, as was done in the study of Oh et al. (2014). By using PVtdT mice, we were able to generate such an areal map for each mouse (Figure S1C). Although the parcellation by Oh et al. (2014) relied on different, presumably structural features in background fluorescence, the overall layout of the CCF and the parcellation used in the present study are notably similar (Figures S1A and S1B). Nevertheless, because we found a different connection density than Oh et al. (2014), it is important to consider whether this may be attributable to differences in parcellation schemes. Comparing the density observed in the two parcellation schemes gives an estimation of the relative accuracy of the density measure and its sensitivity to small changes in parcellation. Analysis of the present data using the parcellation of Oh et al. (2014) yielded a density of 95.7%, nearly identical to that of the present study (97.4%) (Figure S6). Further, our analysis of the raw anterograde data generated by Oh et al. (2014) revealed an ultra-dense network of 90.1% (see Partial Coverage and Global Claims in the STAR Methods). Hence, the minor parcellation differences did not have a significant effect on connection density, regardless of whether it was derived by anterograde studies (Oh et al., 2014) or retrograde tracing (this study). Nevertheless, referencing connections to the individually derived map rather than a template may account for the higher consistency of connectivity profiles in the present study.

A second aim of our study was to compare the cortical graph density of mouse and macaque. Given the large differences in brain size, one possible concern is that the mouse injections might occupy a larger fraction of each area, encompassing local connectional heterogeneities (Falchier et al., 2002; Malach, 1989) and, hence, labeling a larger proportion of the total afferents to the injected area. We consider this unlikely to be a major factor, however, because measurements of injection sites showed that, relative to brain size (Sincich et al., 2003; Stevens, 1989), the volumes of DY injections in mouse and macaque were similar (Figure S7). Another concern is that the longer distances in the larger macaque brain may lead to suboptimal labeling of widely separated areas. Elsewhere, we have argued that this is unlikely, given that survival times exceed the active retrograde transport times required and that the intensity of individual cell labeling does not decline discernibly with increases in distance (Markov et al., 2014a).

## Functional Implications of the Present Results

Graph density is an important measure of the level of connectivity in a network. Although many networks are sparse (e.g., social networks, technological/information technology [IT] networks, infrastructure networks, gene regulatory networks, metabolic networks, and protein interaction networks), cortical interareal networks, surprisingly, form high-density graphs. A graph is considered sparse when the number of links is of the same order as the number of nodes; for example, a network of 19 nodes would be sparse when it has 20∼50 directed links, not the 334 reported here. The high-density character of the cortical network was first reported in the macaque, with a graph density of 66% (Markov et al., 2011). The current data, obtained with the same deterministic approach, reveal an ultra-dense mouse interareal network (97% density, nearly a complete graph). It is consistent with a predicted decrease in density with increasing brain size (Ringo, 1991). The much-expanded human cortex has a reported 180 areas per hemisphere (Glasser et al., 2016), about 4-fold greater than the 41 reported here for the mouse and more than the ∼130 areas reported for the macaque (Van Essen et al., 2012). An intriguing but unresolved question is whether the human cortex might exhibit network sparsity, resulting in specific structural and functional consequences as well as an increased susceptibility to disconnection syndromes (Bullmore and Sporns, 2012; Friston and Frith, 1995; Horvát et al., 2016).

The high cortical density implies that almost all area pairs in the mouse have direct connectivity, *both ways*, suggesting high integration of information across the entire cortical network. Although, at such high densities, specificity is lacking for the purely binary graph, it is restored when we take into account the weights of the connections. Inspection of the weighted connectivity matrix in Figure 7B demonstrates striking asymmetries in many bidirectional connectivity strengths, showing that $G_{19x19}$ is a directed graph with strong weight specificity. This is also evident from a comparison of individual tracer injections; for example, V1 injections show sparse labeling of somatosensory sub-areas, whereas somatosensory injections show much stronger labeling in V1. To decipher processing and information flow in such networks, one must use methods that exploit the weighted nature of connections (Barrat et al., 2004; Newman, 2004) and the geometrical and morphological features of the areas within the cortical plate.

Despite its small size (0.4 g in weight), the mouse brain has become an increasingly important model for investigating higher functions of the cortex using sophisticated methods that enable unprecedented progress in neuroscience. The fact that the mouse cortex has a graph density of 97% strongly affects how we understand the relationship between the structure and function of the cortex. The mouse cortical graph can achieve a high functional specificity despite its high density because each area has distinct connectivity profiles (Bressler and Menon, 2010; Markov et al., 2013a; Passingham et al., 2002). Comparison of the present results with findings in the macaque (Markov et al., 2011, 2014a) shows specificity of the connectivity profiles, reflecting similar levels of variability in both species.

There are multiple origins of variability of cortical connectivity. The number of cortical areas in an ancestral mammal common to rodents and primates is not known, but evolution evidently led to an increase in the number of cortical areas in the primate lineage (especially humans) compared with the rodent/mouse lineage (Kaas, 2000; Striedter, 2005). Evolutionary changes include a relative increase in the extent of the cortical mantle that is referred to as the association cortex in primates (i.e., the cortex outside of the early sensory/motor areas) (Sousa et al., 2017). Cortical development is known to be under both intrinsic and extrinsic factors. Environmental factors that are known to influence the development of the cortex (Kennedy and Dehay, 1993; O'Leary et al., 2007) could potentially have a differential effect on arealization and variability in cortical connectivity in mouse and macaque (Buckner and Krienen, 2013). Further, the laboratory mouse is a highly inbred strain that may exhibit less phenotypic variability than the macaque.

Many of the connections linking cortical areas show very low weights. Nevertheless, weak projections show good consistency both in mouse (present study) and macaque (Markov et al., 2011, 2013a, 2013b). Although the role of weak connections in brain networks is unknown, in social and aging biological networks, the loss of weak connections may render the system unstable (Csermely, 2006; Granovetter, 1973). A similar hypothesis was used in theoretical analysis of the macaque cortical connectome (Goulas et al., 2015) and in recent imaging data in humans (Bassett and Bullmore, 2016). Our confirmation that weak connections are consistent in the mouse highlights the importance of considering them in large-scale models of brain networks.

What does all this tell us about neural function? The combination of a high-density and marked connectivity profiles affirms the specificity of the mouse cortical graph but nevertheless suggests a comparatively high redundancy in the mouse cortex compared with larger brains, which are predicted to be sparse (Horvát et al., 2016). Future analysis of the weighted features of high- and low-density cortical graphs may suggest which features are invariant and which have adaptive value. These lines of research, exploring the network properties of the small and large brain and informed by differences in scaling rules across rodents and primates (Ventura-Antunes et al., 2013), are part of the emerging field of comparative connectomics (Horvát et al., 2016; van den Heuvel et al., 2016; Wang and Kennedy, 2016). The present study provides a weighted, edge-complete subgraph of the mouse cortex that will facilitate the development of

comparative models across species. To the extent that such graphs are based on a uniform coverage of the cortex, the results computed on them should be representative of the expected values for the full connectome. They also serve as templates on which models of the cortex can be implemented and the results compared among them and with those from the data (Ercsey-Ravasz et al., 2013; Horvát et al., 2016; Noori et al., 2017; Song et al., 2014). This will be important for assessing the limitations of the rodent model for understanding the human brain. For example, the dense network linking the primary sensory areas in the mouse have only a limited anatomical counterpart in primates and might dictate a rodent-specific multimodal sensory integration process (Lee and Whitt, 2015; Olcese et al., 2013; Teichert and Bolz, 2017). Finally, these data will also facilitate the application of network control frameworks to help predict the neural function of diverse network modules (Yan et al., 2017).

## STAR★METHODS

Detailed methods are provided in the online version of this paper and include the following:

- KEY RESOURCES TABLE
- CONTACT FOR REAGENT AND RESOURCE SHARING
- EXPERIMENTAL MODEL AND SUBJECT DETAILS
  - Animals
- METHOD DETAILS
  - Abbreviations
  - Tracer injections
  - Suitability of DY Tracing
  - Histology
  - Processing of labeled neurons
  - Parcellation of the cortex
- QUANTIFICATION AND STATISTICAL ANALYSIS
  - Computation of FLNe
  - Overdispersion
  - Accordance with the negative binomial model
  - Variability and consistency
  - Evaluating Akaike Information Criterion
  - Overdispersion and connectivity profiles
  - Processing Oh et al. (2014) data
  - Network density
  - Partial coverage and global claims
  - In-degree analysis for retrograde data
  - Network communication efficiency
- DATA AND SOFTWARE AVAILABILITY

## SUPPLEMENTAL INFORMATION

Supplemental Information includes eight figures and six tables and can be found with this article online at https://doi.org/10.1016/j.neuron.2017.12.037.

## ACKNOWLEDGMENTS

We thank Bianca Gămănuț and Katia Valkova for excellent technical assistance. This work was supported by LABEX CORTEX (ANR-11-LABX-0042) of the Université de Lyon (ANR-11-IDEX-0007) operated by the French National Research Agency (ANR) (to H.K.), ANR-14-CE13-0033-ARCHI-CORE (to H.K.), ANR-15-CE32-0016-CORNET (to H.K.), ANR-17-NEUC-0004-A2P2MC (to H.K. and Z.T.), National Science Foundation (NSF) grant IIS-1724297 (to Z.T. and H.K.), ANR-17-FLAG-ERA-HBP-CORTICITY (to H.K., M.E.-R., and Z.T.), the Fédération des Aveugles de France (to R.G.), the McDonnell Center for Systems Neuroscience grant 22-3920-26239J (to A.B. and R.G.), NIH grants RO1 EY022090 (to A.B.) and R01MH060974 (to D.C.V.E.), and EU-H2020 grant 668863-SyBil-AA (to M.E.-R.).

## AUTHOR CONTRIBUTIONS

H.K. proposed the research. H.K. and A.B. designed the experiments. R.G. and A.B. performed the experiments. R.G., H.K., Z.T., M.E.-R., and K.K. analyzed the data. H.K., Z.T., K.K., and A.B. wrote the first draft. R.G., H.K., Z.T., M.E.-R., D.C.V.E., K.K., and A.B. edited and improved the document over multiple revisions.

## DECLARATION OF INTERESTS

The authors declare no competing interests.

Received: May 2, 2017
Revised: August 30, 2017
Accepted: December 22, 2017
Published: February 7, 2018

## REFERENCES

Akaike, H. (1974). A new look at the statistical model identification. IEEE Trans. Automat. Contr. *19*, 716–723.

Alstott, J., Panzarasa, P., Rubinov, M., Bullmore, E.T., and Vértes, P.E. (2014). A unifying framework for measuring weighted rich clubs. Sci. Rep. *4*, 7258.

Barrat, A., Barthélemy, M., Pastor-Satorras, R., and Vespignani, A. (2004). The architecture of complex weighted networks. Proc. Natl. Acad. Sci. USA *101*, 3747–3752.

Bassett, D.S., and Bullmore, E.T. (2016). Small-world brain networks revisited. Neuroscientist, 1073858416667720.

Beaudin, S.A., Singh, T., Agster, K.L., and Burwell, R.D. (2013). Borders and comparative cytoarchitecture of the perirhinal and postrhinal cortices in an F1 hybrid mouse. Cereb. Cortex *23*, 460–476.

Binzegger, T., Douglas, R.J., and Martin, K.A. (2004). A quantitative map of the circuit of cat primary visual cortex. J. Neurosci. *24*, 8441–8453.

Bota, M., Sporns, O., and Swanson, L.W. (2015). Architecture of the cerebral cortical association connectome underlying cognition. Proc. Natl. Acad. Sci. USA *112*, E2093–E2101.

Bressler, S.L., and Menon, V. (2010). Large-scale brain networks in cognition: emerging methods and principles. Trends Cogn. Sci. *14*, 277–290.

Buckner, R.L., and Krienen, F.M. (2013). The evolution of distributed association networks in the human brain. Trends Cogn. Sci. *17*, 648–665.

Bullier, J., Kennedy, H., and Salinger, W. (1984). Branching and laminar origin of projections between visual cortical areas in the cat. J. Comp. Neurol. *228*, 329–341.

Bullier, J., Kennedy, H., and Salinger, W. (1984a). Bifurcation of subcortical afferents to visual areas 17, 18, and 19 in the cat cortex. J. Comp. Neurol. *228*, 309–328.

Bullier, J., Dehay, C., and Dreher, B. (1990). Bihemispheric axonal bifurcation of the afferents to the visual cortical areas during postnatal development in the rat. Eur. J. Neurosci. *2*, 332–343.

Bullmore, E., and Sporns, O. (2012). The economy of brain network organization. Nat. Rev. Neurosci. *13*, 336–349.

Buzsáki, G., and Mizuseki, K. (2014). The log-dynamic brain: how skewed distributions affect network operations. Nat. Rev. Neurosci. *15*, 264–278.

Carandini, M., and Churchland, A.K. (2013). Probing perceptual decisions in rodents. Nat. Neurosci. *16*, 824–831.

Chen, X., Gabitto, M., Peng, Y., Ryba, N.J., and Zuker, C.S. (2011). A gustotopic map of taste qualities in the mammalian brain. Science *333*, 1262–1266.

Chung, K.L., and AitSahlia, F. (2006). Elementary Probability Theory (Springer).

Condé, F. (1987). Further studies on the use of the fluorescent tracers fast blue and diamidino yellow: effective uptake area and cellular storage sites. J. Neurosci. Methods *21*, 31–43.

Coogan, T.A., and Burkhalter, A. (1993). Hierarchical organization of areas in rat visual cortex. J. Neurosci. *13*, 3749–3772.

Csermely, P. (2006). Weak Links: Stabilizers of Complex Systems from Protein to Social Networks (Springer).

Dehay, C., Kennedy, H., and Bullier, J. (1986). Callosal connectivity of areas V1 and V2 in the newborn monkey. J. Comp. Neurol. *254*, 20–33.

Dehay, C., Kennedy, H., Bullier, J., and Berland, M. (1988). Absence of interhemispheric connections of area 17 during development in the monkey. Nature *331*, 348–350.

Dong, H.W. (2008). The Allen Reference Atlas: A Digital Color Brain Atlas of the C57B1/6J Male Mouse (John Wiley & Sons).

Ercsey-Ravasz, M., Markov, N.T., Lamy, C., Van Essen, D.C., Knoblauch, K., Toroczkai, Z., and Kennedy, H. (2013). A predictive network model of cerebral cortical connectivity based on a distance rule. Neuron *80*, 184–197.

Fabri, M., and Burton, H. (1991). Ipsilateral cortical connections of primary somatic sensory cortex in rats. J. Comp. Neurol. *311*, 405–424.

Falchier, A., Clavagnier, S., Barone, P., and Kennedy, H. (2002). Anatomical evidence of multimodal integration in primate striate cortex. J. Neurosci. *22*, 5749–5759.

Felleman, D.J., and Van Essen, D.C. (1991). Distributed hierarchical processing in the primate cerebral cortex. Cereb. Cortex *1*, 1–47.

Ferezou, I., Haiss, F., Gentet, L.J., Aronoff, R., Weber, B., and Petersen, C.C. (2007). Spatiotemporal dynamics of cortical sensorimotor integration in behaving mice. Neuron *56*, 907–923.

Friston, K.J., and Frith, C.D. (1995). Schizophrenia: a disconnection syndrome? Clin. Neurosci. *3*, 89–97.

Garrett, M.E., Nauhaus, I., Marshel, J.H., and Callaway, E.M. (2014). Topography and areal organization of mouse visual cortex. J. Neurosci. *34*, 12587–12600.

Glasser, M.F., Coalson, T.S., Robinson, E.C., Hacker, C.D., Harwell, J., Yacoub, E., Ugurbil, K., Andersson, J., Beckmann, C.F., Jenkinson, M., et al. (2016). A multi-modal parcellation of human cerebral cortex. Nature *536*, 171–178.

Goulas, A., Schaefer, A., and Margulies, D.S. (2015). The strength of weak connections in the macaque cortico-cortical network. Brain Struct. Funct. *220*, 2939–2951.

Granovetter, M.S. (1973). The strength of weak ties. Am. J. Sociol. *78*, 1360–1380.

Hilbe, J.M. (2007). Negative Binomial Regression (Cambridge University Press).

Horvát, S., Gămănuţ, R., Ercsey-Ravasz, M., Magrou, L., Gămănuţ, B., Van Essen, D.C., Burkhalter, A., Knoblauch, K., Toroczkai, Z., and Kennedy, H. (2016). Spatial embedding and wiring cost constrain the functional layout of the cortical network of rodents and primates. PLoS Biol. *14*, e1002512.

Ichinohe, N., Fujiyama, F., Kaneko, T., and Rockland, K.S. (2003). Honeycomb-like mosaic at the border of layers 1 and 2 in the cerebral cortex. J Neurosci. *23*, 1372–1382.

Issa, J.B., Haeffele, B.D., Agarwal, A., Bergles, D.E., Young, E.D., and Yue, D.T. (2014). Multiscale optical Ca2+ imaging of tonal organization in mouse auditory cortex. Neuron *83*, 944–959.

Janson, S., Luczak, T., and Rucinski, A. (2000). Random Graphs (Wiley-Interscience).

Kaas, J. (2000). Why is brain size so important: design problems and solutions as neocortex gets bigger or smaller. Brain Mind *1*, 7–23.

Kamada, T., and Kawai, S. (1989). An algorithm for drawing general undirected graphs. Inf. Process. Lett. *31*, 7–15.

Keizer, K., Kuypers, H.G.J.M., Huisman, A.M., and Dann, O. (1983). Diamidino yellow dihydrochloride (DY. 2HCl); a new fluorescent retrograde neuronal tracer, which migrates only very slowly out of the cell. Exp. Brain Res. *51*, 179–191.

Kennedy, H., and Bullier, J. (1985). A double-labeling investigation of the afferent connectivity to cortical areas V1 and V2 of the macaque monkey. J. Neurosci. *5*, 2815–2830.

Kennedy, H., and Dehay, C. (1993). Cortical specification of mice and men. Cereb. Cortex *3*, 171–186.

Kennedy, H., Knoblauch, K., and Toroczkai, Z. (2013). Why data coherence and quality is critical for understanding interareal cortical networks. Neuroimage *80*, 37–45.

Kim, H., Ährlund-Richter, S., Wang, X., Deisseroth, K., and Carlén, M. (2016). Prefrontal parvalbumin neurons in control of attention. Cell *164*, 208–218.

Kimura, A., Donishi, T., Okamoto, K., and Tamai, Y. (2004). Efferent connections of "posterodorsal" auditory area in the rat cortex: implications for auditory spatial processing. Neuroscience *128*, 399–419.

Krubitzer, L.A., and Seelke, A.M. (2012). Cortical evolution in mammals: the bane and beauty of phenotypic variability. Proc. Natl. Acad. Sci. USA *109* (*Suppl 1*), 10647–10654.

Kulli, V.R., and Sigarkanti, S.C. (1991). Inverse domination in graphs. Nat. Acad. Sci. Lett. *14*, 473–475.

Latora, V., and Marchiori, M. (2003). Economic small-world behavior in weighted networks. Eur. Phys. J. B *32*, 249–263.

Lee, H.K., and Whitt, J.L. (2015). Cross-modal synaptic plasticity in adult primary sensory cortices. Curr. Opin. Neurobiol. *35*, 119–126.

LeVay, S., and Sherk, H. (1983). Retrograde transport of [3H]proline: a widespread phenomenon in the central nervous system. Brain Res. *271*, 131–134.

Li, N., Daie, K., Svoboda, K., and Druckmann, S. (2016). Robust neuronal dynamics in premotor cortex during motor planning. Nature *532*, 459–464.

MacNeil, M.A., Einstein, G., and Payne, B.R. (1997). Transgeniculate signal transmission to middle suprasylvian cortex in intact cats and following early removal of areas 17 and 18: a morphological study. Exp. Brain Res. *114*, 11–23.

Malach, R. (1989). Patterns of connections in rat visual cortex. J. Neurosci. *9*, 3741–3752.

Manita, S., Suzuki, T., Homma, C., Matsumoto, T., Odagawa, M., Yamada, K., Ota, K., Matsubara, C., Inutsuka, A., Sato, M., et al. (2015). A top-down cortical circuit for accurate sensory perception. Neuron *86*, 1304–1316.

Markov, N.T., Misery, P., Falchier, A., Lamy, C., Vezoli, J., Quilodran, R., Gariel, M.A., Giroud, P., Ercsey-Ravasz, M., Pilaz, L.J., et al. (2011). Weight consistency specifies regularities of macaque cortical networks. Cereb. Cortex *21*, 1254–1272.

Markov, N.T., Ercsey-Ravasz, M., Lamy, C., Ribeiro Gomes, A.R., Magrou, L., Misery, P., Giroud, P., Barone, P., Dehay, C., Toroczkai, Z., et al. (2013a). The role of long-range connections on the specificity of the macaque interareal cortical network. Proc. Natl. Acad. Sci. USA *110*, 5187–5192.

Markov, N.T., Ercsey-Ravasz, M., Van Essen, D.C., Knoblauch, K., Toroczkai, Z., and Kennedy, H. (2013b). Cortical high-density counterstream architectures. Science *342*, 1238406.

Markov, N.T., Ercsey-Ravasz, M.M., Ribeiro Gomes, A.R., Lamy, C., Magrou, L., Vezoli, J., Misery, P., Falchier, A., Quilodran, R., Gariel, M.A., et al. (2014a). A weighted and directed interareal connectivity matrix for macaque cerebral cortex. Cereb. Cortex *24*, 17–36.

Markov, N.T., Vezoli, J., Chameau, P., Falchier, A., Quilodran, R., Huissoud, C., Lamy, C., Misery, P., Giroud, P., Ullman, S., et al. (2014b). Anatomy of hierarchy: feedforward and feedback pathways in macaque visual cortex. J. Comp. Neurol. *522*, 225–259.

Marshel, J.H., Garrett, M.E., Nauhaus, I., and Callaway, E.M. (2011). Functional specialization of seven mouse visual cortical areas. Neuron *72*, 1040–1054.

McCullagh, P., and Nelder, J.A. (1989). Generalized Linear Models, Second Edition (Chapman & Hall/CRC).

Mease, R.A., Metz, M., and Groh, A. (2016). Cortical sensory responses are enhanced by the higher-order thalamus. Cell Rep. *14*, 208–215.

Muldoon, S.F., Bridgeford, E.W., and Bassett, D.S. (2016). Small-world propensity and weighted brain networks. Sci. Rep. *6*, 22057.

Musil, S.Y., and Olson, C.R. (1988a). Organization of cortical and subcortical projections to anterior cingulate cortex in the cat. J. Comp. Neurol. *272*, 203–218.

Musil, S.Y., and Olson, C.R. (1988b). Organization of cortical and subcortical projections to medial prefrontal cortex in the cat. J. Comp. Neurol. *272*, 219–241.

Newman, M.E.J. (2004). Analysis of weighted networks. Phys. Rev. E Stat. Nonlin. Soft Matter Phys. *70*, 056131.

Newman, M.E.J. (2010). Networks: An Introduction (Oxford University Press).

Noori, H.R., Schöttler, J., Ercsey-Ravasz, M., Cosa-Linan, A., Varga, M., Toroczkai, Z., and Spanagel, R. (2017). A multiscale cerebral neurochemical connectome of the rat brain. PLoS Biol. *15*, e2002612.

O'Leary, D.D., Chou, S.J., and Sahara, S. (2007). Area patterning of the mammalian cortex. Neuron *56*, 252–269.

Oh, S.W., Harris, J.A., Ng, L., Winslow, B., Cain, N., Mihalas, S., Wang, Q., Lau, C., Kuan, L., Henry, A.M., et al. (2014). A mesoscale connectome of the mouse brain. Nature *508*, 207–214.

Olcese, U., Iurilli, G., and Medini, P. (2013). Cellular and synaptic architecture of multisensory integration in the mouse neocortex. Neuron *79*, 579–593.

Olson, C.R., and Musil, S.Y. (1992). Topographic organization of cortical and subcortical projections to posterior cingulate cortex in the cat: evidence for somatic, ocular, and complex subregions. J. Comp. Neurol. *324*, 237–260.

Passingham, R.E., Stephan, K.E., and Kötter, R. (2002). The anatomical basis of functional localization in the cortex. Nat. Rev. Neurosci. *3*, 606–616.

Payne, J.N. (1987). Comparisons between the use of true blue and diamidino yellow as retrograde fluorescent tracers. Exp. Brain Res. *68*, 631–642.

Perkel, D.J., Bullier, J., and Kennedy, H. (1986). Topography of the afferent connectivity of area 17 in the macaque monkey: a double-labelling study. J. Comp. Neurol. *253*, 374–402.

Qi, H.X., and Kaas, J.H. (2004). Myelin stains reveal an anatomical framework for the representation of the digits in somatosensory area 3b of macaque monkeys. J. Comp. Neurol. *477*, 172–187.

Reiner, A., Veenman, C.L., Medina, L., Jiao, Y., Del Mar, N., and Honig, M.G. (2000). Pathway tracing using biotinylated dextran amines. J. Neurosci. Methods *103*, 23–37.

Remple, M.S., Henry, E.C., and Catania, K.C. (2003). Organization of somatosensory cortex in the laboratory rat (Rattus norvegicus): Evidence for two lateral areas joined at the representation of the teeth. J. Comp. Neurol. *467*, 105–118.

Ringo, J.L. (1991). Neuronal interconnection as a function of brain size. Brain Behav. Evol. *38*, 1–6.

Rodgers, K.M., Benison, A.M., Klein, A., and Barth, D.S. (2008). Auditory, somatosensory, and multisensory insular cortex in the rat. Cereb. Cortex *18*, 2941–2951.

Saleem, K.S., and Logothetis, N.K. (2012). Atlas of the Rhesus Monkey Brain (Elsevier, Academic Press).

Sawatari, H., Tanaka, Y., Takemoto, M., Nishimura, M., Hasegawa, K., Saitoh, K., and Song, W.J. (2011). Identification and characterization of an insular auditory field in mice. Eur. J. Neurosci. *34*, 1944–1952.

Scannell, J.W., Grant, S., Payne, B.R., and Baddeley, R. (2000). On variability in the density of corticocortical and thalamocortical connections. Philos. Trans. R. Soc. Lond. B Biol. Sci. *355*, 21–35.

Sherman, S.M. (2016). Thalamus plays a central role in ongoing cortical functioning. Nat. Neurosci. *19*, 533–541.

Sincich, L.C., Adams, D.L., and Horton, J.C. (2003). Complete flatmounting of the macaque cerebral cortex. Vis. Neurosci. *20*, 663–686.

Song, S., Sjöström, P.J., Reigl, M., Nelson, S., and Chklovskii, D.B. (2005). Highly nonrandom features of synaptic connectivity in local cortical circuits. PLoS Biol. *3*, e68.

Song, H.F., Kennedy, H., and Wang, X.J. (2014). Spatial embedding of structural similarity in the cerebral cortex. Proc. Natl. Acad. Sci. USA *111*, 16580–16585.

Sousa, A.M.M., Meyer, K.A., Santpere, G., Gulden, F.O., and Sestan, N. (2017). Evolution of the human nervous system: function, structure, and development. Cell *170*, 226–247.

Sporns, O., and Zwi, J.D. (2004). The small world of the cerebral cortex. Neuroinformatics *2*, 145–162.

Stevens, C.F. (1989). How cortical interconnectedness varies with network size. Neural Comput. *1*, 473–479.

Striedter, G.F. (2005). Principles of Brain Evolution (Sinauer Associates).

Tanahira, C., Higo, S., Watanabe, K., Tomioka, R., Ebihara, S., Kaneko, T., and Tamamaki, N. (2009). Parvalbumin neurons in the forebrain as revealed by parvalbumin-Cre transgenic mice. Neurosci. Res. *63*, 213–223.

Teichert, M., and Bolz, J. (2017). Simultaneous intrinsic signal imaging of auditory and visual cortex reveals profound effects of acute hearing loss on visual processing. Neuroimage *159*, 459–472.

Tsukano, H., Horie, M., Hishida, R., Takahashi, K., Takebayashi, H., and Shibuki, K. (2016). Quantitative map of multiple auditory cortical regions with a stereotaxic fine-scale atlas of the mouse brain. Sci. Rep. *6*, 22315.

Van De Werd, H.J., Rajkowska, G., Evers, P., and Uylings, H.B. (2010). Cytoarchitectonic and chemoarchitectonic characterization of the prefrontal cortical areas in the mouse. Brain Struct. Funct. *214*, 339–353.

van den Heuvel, M.P., Bullmore, E.T., and Sporns, O. (2016). Comparative connectomics. Trends Cogn. Sci. *20*, 345–361.

Van Essen, D.C. (2003). Organization of visual areas in macaque and human cerebral cortex. In The Visual Neurosciences, L.M. Chalupa and J.S. Werner, eds. (MIT Press), pp. 507–521.

Van Essen, D.C., Glasser, M.F., Dierker, D., and Harwell, J. (2012). Cortical parcellations of the macaque monkey analyzed on surface-based atlases. Cereb Cortex. *22*, 2227–2240.

Ventura-Antunes, L., Mota, B., and Herculano-Houzel, S. (2013). Different scaling of white matter volume, cortical connectivity, and gyrification across rodent and primate brains. Front. Neuroanat. *7*, 3.

Vragović, I., Louis, E., and Díaz-Guilera, A. (2005). Efficiency of informational transfer in regular and complex networks. Phys. Rev. E Stat. Nonlin. Soft Matter Phys. *71* (3 Pt 2A), 036122.

Wang, Q., and Burkhalter, A. (2007). Area map of mouse visual cortex. J. Comp. Neurol. *502*, 339–357.

Wang, X.-J., and Kennedy, H. (2016). Brain structure and dynamics across scales: in search of rules. Curr. Opin. Neurobiol. *37*, 92–98.

Wang, Q., Gao, E., and Burkhalter, A. (2007). In vivo transcranial imaging of connections in mouse visual cortex. J. Neurosci. Methods *159*, 268–276.

Wang, Q., Gao, E., and Burkhalter, A. (2011). Gateways of ventral and dorsal streams in mouse visual cortex. J. Neurosci. *31*, 1905–1918.

Wang, Q., Sporns, O., and Burkhalter, A. (2012). Network analysis of corticocortical connections reveals ventral and dorsal processing streams in mouse visual cortex. J. Neurosci. *32*, 4386–4399.

Wang, Q., Henry, A.M., Harris, J.A., Oh, S.W., Joines, K.M., Nyhus, J., Hirokawa, K.E., Dee, N., Mortrud, M., Parry, S., et al. (2014). Systematic comparison of adeno-associated virus and biotinylated dextran amine reveals equivalent sensitivity between tracers and novel projection targets in the mouse brain. J. Comp. Neurol. *522*, 1989–2012.

Yamashita, A., Valkova, K., Gonchar, Y., and Burkhalter, A. (2003). Rearrangement of synaptic connections with inhibitory neurons in developing mouse visual cortex. J. Comp. Neurol. *464*, 426–437.

Yan, G., Vértes, P.E., Towlson, E.K., Chew, Y.L., Walker, D.S., Schafer, W.R., and Barabási, A.L. (2017). Network control principles predict neuron function in the Caenorhabditis elegans connectome. Nature *550*, 519–523.

Ypma, R.J., and Bullmore, E.T. (2016). Statistical analysis of tract-tracing experiments demonstrates a dense, complex cortical network in the mouse. PLoS Comput. Biol. *12*, e1005104.

Zhuang, J., Ng, L., Williams, D., Valley, M., Li, Y., Garrett, M., and Waters, J. (2017). An extended retinotopic map of mouse cortex. eLife *6*, e18372.

Zingg, B., Hintiryan, H., Gou, L., Song, M.Y., Bay, M., Bienkowski, M.S., Foster, N.N., Yamashita, S., Bowman, I., Toga, A.W., and Dong, H.W. (2014). Neural networks of the mouse neocortex. Cell *156*, 1096–1111.

# STAR★METHODS

## KEY RESOURCES TABLE

| REAGENT or RESOURCE | SOURCE | IDENTIFIER |
|---|---|---|
| Antibodies | | |
| M2 | Millipore | Cat# MAB367, RRID:AB_94952 |
| VGluT2 | Millipore | Cat# AB2251-I, RRID:AB_2665454 |
| Deposited Data | | |
| FLNe data | This paper | http://www.core-nets.org/ |
| Experimental Models: Organisms/Strains | | |
| Mouse C57BL/6J | The Jackson Laboratory | Cat# JAX:000664, RRID: IMSR_JAX:000664 |
| Mouse B6.*129P2-Pvalb*$^{tm1(cre)Arbr/J}$ | The Jackson Laboratory | Cat# JAX:008069, RRID: IMSR_JAX:008069 |
| Mouse B6;129S6-*Gt(ROSA)26Sor*$^{tm9(CAG)tdTomato)Hze}$/J | The Jackson Laboratory | Cat# JAX:007905, RRID: IMSR_JAX:007905 |
| Mouse *Slc17a6*$^{tm2(cre)Lowl}$/J | The Jackson Laboratory | Cat# JAX:016963, RRID: IMSR_JAX:016963 |
| Mouse B6;*Cg-Chrm2*$^{tm1.Hze}$/J | The Jackson Laboratory | Cat# JAX:030330, RRID: IMSR_JAX:030330 |
| Software and Algorithms | | |
| Mercator | Explora Nova | http://www.exploranova.com |
| MorphoStrider | Explora Nova | http://www.exploranova.com |
| Adobe Illustrator CS5 | Adobe Systems | http://www.adobe.com |
| Python 2.7 | Python Software Foundation | http://www.python.org/ |
| R | R core team | http://ww1.r-project.com |
| Pajek | Vladimir Batagelj, Andrej Mrvar | http://mrvar.fdv.uni-lj.si/pajek/ |
| Akaike's Information Criterion | Akaike, 1974 | https://stat.ethz.ch/R-manual/R-devel/library/stats/html/AIC.html |
| Generalized linear model | McCullagh and Nelder, 1989 | https://stat.ethz.ch/R-manual/R-devel/library/stats/html/glm.html |
| Kamada-Kawai force-based algorithm | Kamada and Kawai, 1989 | http://mrvar.fdv.uni-lj.si/pajek/ |
| Other | | |
| Diamidino Yellow | EMS-Chemie, Gross-Umstadt, Germany | http://www.ems-group.de |
| Mouse anterograde projections raw data | Allen Brain Institute | Oh et al., 2014 |
| Mouse anterograde projections computed data | Allen Brain Institute | Oh et al., 2014 |

## CONTACT FOR REAGENT AND RESOURCE SHARING

Further information and requests for reagents and resource may be directed to the Lead Contact, Henry Kennedy (henry.kennedy@inserm.fr).

## EXPERIMENTAL MODEL AND SUBJECT DETAILS

### Animals

Retrograde tracing experiments with Diamidino Yellow (DY), immunostaining for M2 muscarinic acetylcholine receptor (M2), vesicular glutamate transporter 2 (VGluT2) and cytochrome oxidase (CO) histochemistry were performed in 141 male and female mice. 33 C57BL/6J (Jackon Lab) (of which 14 injected with DY, 3 of which successful for this study; 19 used for immunostaining and histochemistry); 88 PV-Cre (B6.*129P2-Pvalb*$^{tm1(cre)Arbr}$/J, Jackson Lab) x Ai9 (B6;129S6-*Gt(ROSA)26Sor*$^{tm9(CAG-tdTomatoHze}$/J, Jackson Lab) of which 24 successful for DY labeling in this study; 8 for fluorescence imaging of VGluT2 (*Slc17a6*$^{tm2(cre)Lowl}$/J, Jackson Lab); and 12 for fluorescence imaging of M2 (B6;*Cg-Chrm2*$^{tm1.Hze}$/J, Jackson Lab). All experimental procedures were approved by the institutional Animal Care and Use Committee at Washington University.

For the 27 mice which were successfully injected, the age span is 8-30 weeks, and sex is known for only 2 cases, both females (Table S6). The others are mostly males, for technical reasons – females being retained for breeding. Sex was not registered because there are no known sex differences in cortical connectivity.

## METHOD DETAILS

### Abbreviations

A - Anterior area
ABI – Allen Institute for Brain Science
ACAd, ACAv - Anterior cingulate area dorsal part, ventral part
AIC – Akaike Information Criterion
AId, AIv, AIp - Agranular insular area dorsal part, ventral part, posterior part
AL – Anterolateral area
AM - Anteromedial area
AMY - Amygdala
AOB - Accessory olfactory bulb
AON - Anterior olfactory nucleus
ARA – Allen Reference Atlas
AUDp, AUDpo, AUDv - Auditory cortex primary area, posterior area, ventral area
CCF – Common Reference Frame
CoA – Cortical amygdala
DP - Dorsal posterior area (also known as PD; Kimura et al., 2004)
DY – Diamidino Yellow
ECT - Ectorhinal area (also referred to as area 36; Beaudin et al., 2013)
EDR – Exponential distance rule, which is the negative exponential dependence of weights on distance (Ercsey-Ravasz et al., 2013)
ENTl, ENTm - Entorhinal area lateral part, medial part
FIN - Full interareal network ($G_{47x47}$)
FLNe – extrinsic Fraction of Labeled Neurons
FRP - Frontal pole
GU - Gustatory area
$G_{19x19}$, $G_{47x47}$, $G_{19x47}$ – Cortical graphs (*number of target areas* X *number of source areas*)
HPF - Hippocampal formation
ILA - Infralimbic area
IT – Information technology
$< k >_{in}$ – Average in-degree (average number of source areas projecting to a target area)
LI - Laterointermediate area
LLA - Laterolateral anterior area
LM - Lateromedial area
M, $M_{FIN}$ – The number of directed links in $G_{19x19}$ and $G_{47x47}$, respectively
MDS – Minimum Dominating Set
MM - Mediomedial area
MOp, MOs - Motor cortex primary, secondary
N, $N_{FIN}$ - The number of nodes in $G_{19x19}$ and $G_{47x47}$, respectively
NLOT – Nucleus lateral olfactory tract
OB - Olfactory bulb
OT - Olfactory tubercle
ORBl, ORBm - Orbitofrontal area lateral part, medial part
P - Posterior area
ParS - Parasubiculum
PERI - Perirhinal area (also referred to as area 35; Beaudin et al., 2013)
Pir - Piriform cortex
PL - Prelimbic area
PM - Posteromedial area
POR - Postrhinal area
PORa – Postrhinal anterior (previously annotated as 36p; Wang et al., 2011)
PreS – Presubiculum
PV - Parvalbumin

rf – Rhinal sulcus
RL - Rostrolateral area
RSPagl, RSPd, RSPv - Retrosplenial area agranular part, dorsal part, ventral part
$\rho$, $\rho_{FIN}$ - The densities of the directed graphs $G_{19x19}$ and $G_{47x47}$, respectively
SBRI – Stem Cell and Brain Research Institute
SSp - Somatosensory cortex primary (barrel field [SSp-bfd], lower jaw [SSp-lj], lower limb [SSp-ll], upper limb [SSp-ul], trunk [SSp-tr], nose and mouth [SSp-nm])
SSs - Somatosensory cortex secondary
SUB – Subiculum
tdT - tdTomato
TEa, TEp -Temporal area anterior part, posterior part
TR - Postpiriform transition area
V1 – Primary visual area
VISC - Visceral area
VISa - Visual anterior
VISal - Visual anterolateral
VISam - Visual anteromedial
VISli - Visual intermediolateral
VISlm - Visual lateromedial
VISp - Visual primary
VISpl - Visual posterolateral
VISpm - Visual posteromedial
VISpost - Visual postrhinal

## Tracer injections

Prior to tracer injection, mice were anesthetized with a mixture of Ketamine (86 mg · kg −1) and Xylazine (13 mg · kg-1, i.p) and secured in a headholder. Body temperature was maintained at 37°C. Left-hemisphere tracer injections were made by inserting a glass pipette (20 μm tip diameter) through the dura into the brain and injecting DY (50 nl, 2% in $H_2O$; EMS-Chemie, Gross-Umstadt, Germany) by pressure (Picospritzer, Parker-Hannafin). Injections were aimed stereotaxically 0.35 mm below the pial surface and often required pulling back the pipette to correct proportionally for dimpling of the dura and confining potential injury to layers 1-4. Cases in which injected DY spilled into the white matter or across areal borders were excluded from the study. From a total of 102 DY injections, 27 were successfully confined to 17 distinct areas and two subareas of SSp (Figures 2A–2F). The origin of the coordinate system was the intersection between the midline and a perpendicular line drawn from the anterior border of the transverse sinus at the posterior pole of the occipital cortex. The injection sites identified as 120-280 μm-wide crystalline deposits of DY (Figures 2A, 2D, and 2F) of occipital, temporal, insular, parietal, restrosplenial, motor, cingulate and prefrontal cortex. Their details are the following, specifying the injected area, the anterior/lateral position in mm, and the number of successfully injected animals: ACAd (6/0.1, n = 1), AL (2.4/3.7, n = 1) (Figure 2E), AM (3/1.7, n = 2), AUDpo (2.3/5, n = 1), DP (4.5/2, n = 1), GU (6/4, n = 1), LM (1.4/4.2, n = 3) (Figure 2D), MM (1.9/1.6, n = 1), MOp (6.45/2, n = 1), P (0.7/4.1, n = 1), PL (6.8/0.1, n = 1), PM (1.9/1.6, n = 1) (Figure 2F), RL (2.8/3.3, n = 2), RSPd (2.1/0.4, n = 1), SSp-bfd (3.4/3.25, n = 2), SSp-un (3.4/2.4, n = 1), SSs (3.75/3.25, n = 1), V1 (1.1/2.4-2.9, n = 4) (Figures 2A–2C), VISC (4.2/4.5, n = 1). Note that under fluorescence illumination, injection sites appeared larger, but nevertheless showed no apparent spread to neighboring areas. In all cases, retrograde DY labeling was very bright and labeled large numbers of neurons in multiple areas distributed across the cortex.

## Suitability of DY Tracing

The choice of a highly sensitive retrograde tracer was crucial. In contrast to tracers such as FluoroGold and Cholera Toxin B, DY is predominantly a nuclear stain, which means that labeling is dense and spot-like (Figure S2B) and lacks the ambiguities introduced by the often fragmented appearance of cytoplasmically labeled neurons. Hence, high-density labeling, such as found in the present project, can be accurately mapped out and the full range of labeling density successfully captured (Figure S2B).

How reliable is DY tracing with respect to sensitivity, restriction of pick-up zone and minimization of false positives?

First, the reason for using DY was to enable direct comparison of cortical connectivity in mouse and monkey. The identification of projections that were previously unknown (Markov et al., 2014b) has shown that DY is a non-selective tracer which preferentially labels nuclei of projection neurons (Condé, 1987) with superior efficiency.

Second, importantly, DY has a highly restricted and identifiable pick-up zone making it possible to identify the area effectively injected with great precision. DY was taken up from a crystalline bolus deposited in the cortex, which in the present study was 120-280 μm in diameter (Figure 2). Such injections were small enough to be confined to the tiny areas of the mouse cortex, but sufficiently large to overcome possible connectional heterogeneities within an area that may cause between-injection variability (MacNeil et al., 1997; Scannell et al., 2000). Because experiments in monkey have shown that the bolus diameter roughly

corresponds to the DY-uptake zone (Bullier et al., 1984a; Condé, 1987; Kennedy and Bullier, 1985; Perkel et al., 1986), we are confident that in all the reported cases here DY was captured from within a given area. To exclude DY-uptake through injured fibers we have further confined injections to layer 1-4 and thus, minimized labeling through damaged fibers of passage between different cortical areas (Yamashita et al., 2003), but allowing uptake of spreading tracer by terminals projecting to layers 5 and 6. Uptake by intact fibers of passage is rare and inefficient (Payne, 1987).

Thirdly, the problem of false positives is well defined with DY. Leakage of DY from backlabeled neurons *in vivo* is negligible (Keizer et al., 1983) and we have argued elsewhere with respect to published results that there is no evidence that secondary pick-up leads to false positives with this tracer (Markov et al., 2011, 2014a). For instance the lack of secondary uptake in cortex (Bullier et al., 1990, 1984, 1984a; Markov et al., 2014b) was most convincingly shown by the failure of labeling transcallosal projection neurons in monkey V1 after injection of DY in contralateral V2, which failed to label cells in the unconnected region of V1, away from the heavily connected strip along the V1/V2 border (Dehay et al., 1986, 1988). Release and secondary pick-up is rare for fixed, floating sections, but as a precaution of secondary labeling sections were immediately mounted on glass slides, air-dried and stored at −20°C until analysis under fluorescence optics. Taken together it seems highly unlikely that, following retrograde transport to the source area, DY was released and picked up by neurons in quantities sufficient to produce secondary labeling.

Fourthly, for comparison, anterograde labeling with viral (Oh et al., 2014) and non-viral tracers (Zingg et al., 2014) can lead to a category of false positives that do not occur in retrograde DY tracing and complicate the interpretation of results. These include retrograde labeling of neurons and their local axon collaterals in the projection target (LeVay and Sherk, 1983; Wang et al., 2014). Such contamination may explain false positive cortical inputs from the superior colliculus and pontine nucleus observed by Oh et al. (2014).

### Histology

Four days after tracer injection, mice were euthanized with Ketamine/Xylazine and perfused through the heart with phosphate buffered saline, followed by 1% paraformaldehyde (PFA) in 0.1M phosphate buffer (PB, pH 7.4). The cortex was immediately separated from the rest of the brain. To unfold and flatten the cortex, the tissue was placed on a glass surface, pial surface down. Using microsurgical knives, the hippocampus was disconnected from neocortex along the seam between alveus and cingulate bundle, and flipped outward while still attached to the entorhinal cortex. A small incision was made to separate medial from lateral orbital cortex. Proceeding in a posterior direction the white matter was split between the corpus callosum and the cingulate bundle, enabling the unfolding of the medial wall containing medial orbital, prefrontal, cingulate, and retrosplenial cortex. The tissue was then transferred white matter down onto a filter paper covering a sponge and weighed down by a glass slide placed on top. The assembly was postfixed in a Petri dish filled with 4% PFA and stored overnight at 4°C. After postfixation the tissue was cryoprotected in 30% sucrose and 40 μm thick sections were cut on a freezing microtome in the tangential plane.

In order to assign in each mouse the injection site and DY labeled neurons to individual cortical areas, we developed a parcellation scheme based on the distinctive distribution of PVtdT expression (see Parcellation of the Cortex below). This eliminated counterstaining for additional areal markers, thereby avoiding loss of signal and the associated risk of secondary labeling by leakage from retrogradely DY labeled cells (see Suitability of DY Tracing above). To determine the reliability of PVtdT in distinguishing distinct parcels, we compared PVtdT borders to borders observed with M2, VGluT2 and CO reactivity, all of which have been employed previously to parcellate rodent cortex (Ichinohe et al., 2003; Wang et al., 2011, 2012). In order to compare all four patterns we used flatmounted PVtdT-expressing sections reacted with antibodies against M2 (MAB367, Millipore) or VGluT2 (AB2251, Millipore) using fluorescent secondary antibodies for visualization. Alternatively, we used tdT fluorescence or non-fluorescent immunohistochemical ABC staining methods to visualize M2 or VGluT2 expression, with histochemistry to reveal CO reactivity. In each case, alternate sections were stained for Nissl substance to reveal the cytoarchitectonic landmarks annotated in the Allen Brain Atlas. The expression patterns were imaged under a microscope equipped for brightfield and fluorescence illumination.

### Processing of labeled neurons

Sections were mounted onto glass slides and DY labeling was analyzed under UV fluorescence (excitation: 355-425 nm, emission: 470 nm) at 20 ×, with a microscope controlled through a computer using the Mercator software package, running on ExploraNova technology. This software enables the observer to manually tag individual neurons at high magnification, extensively using the Z axis to focus on individual labeled cells (Figure S2B). High-fidelity digital charts of the coordinates of labeled neurons were made for all 12–24 sections per hemisphere and digitally stored (Figure S2A). Once charting was complete, sections were imaged for PVtdT (excitation 520-600 nm, emission 570-720 nm) (Figure 2), stained for Nissl substance with Cresyl Violet, and imaged under bright field illumination. The images of the sections were acquired using MorphoStrider software (ExploraNova). We have extensive experience with DY as a retrograde tracer (see Suitability of DY Tracing above). The manual charting of neurons as described above (Figure S2B) minimizes false positives.

The digitized charts of labeled neurons and the images of the corresponding sections were aligned in Adobe Illustrator. The sets of images from each brain were parcellated using the regional patterns in PVtdT expression and Nissl stained cell bodies. This allowed the creation of an individual template at layer 4 for each brain, which was then aligned via adjacent section to superficial and deep layers by matching blood vessels.

## Parcellation of the cortex

Our choice of PVtdT expression for areal identification was inspired by the work of Saleem and Logothetis (2012), who successfully used PV immunostaining to delineate cortical areas in rhesus monkey. However, there is no *a priori* reason to assume that the expression pattern of PVtdT outlines areal boundaries in the mouse. As this is of course true for any individual architectonic marker, we compared the pattern of PVtdT expression with those of immunolabeling for M2, VGluT2, histochemical reactivity for CO, and Nissl staining. Based on previous observations (Wang et al., 2011), our expectation was that comparing different markers would reveal overlapping or complementary spatial expression gradients reflecting areal borders across individuals. The excellent alignment of markers in, for example layer 4 of V1 and SSp (Figure 1) affirms the utility of the PVtdT borders for delimiting areas.

What follows explains how, in tangential sections through layer 2-5, overlapping or complementary patterns of M2, VGluT2 and CO labeling, and overlaying visuotopically mapped areas (Wang and Burkhalter, 2007) to stained landmarks were used to further subdivide the 25 parcels identified by PVtdT expression (Figure 1A, white dashed outlines). Although the PVtdT map was less detailed than the 36 areas annotated in the CCF (Figures S1A and S1C), the overall layout, shapes and sizes of multiple parcels of our atlas is notably similar (Figure S1B). Moreover 19 of the parcels shown in the PVtdT map were simple (i.e., showed no additional subdivisions except for subfields of body parts in SSp) (Figure 1A, black dashed lines), and closely matched those marked positively or negatively by M2, VGluT2 and CO (Figures 1B–1D and S1C–S1F). These included: V1, SSp, SSs, AUDp, GU (Chen et al., 2011; previously annotated as the tooth/tongue representation of SSp; Remple et al., 2003; Wang et al., 2012), VISC (previously referred to as posteroventral area; Fabri and Burton, 1991; Wang et al., 2012; also known as insular auditory field or insular somatosensory field; Rodgers et al., 2008; Sawatari et al., 2011). Further, areas identified by PVtdT-expression alone included the posterior (AIp), ventral (AIv) and dorsal (AId) agranular insular areas (Van De Werd et al., 2010), ACAd, ACAv (Tanahira et al., 2009; Van De Werd et al., 2010), PL and ILA (Van De Werd et al., 2010), FRP (ARA), ORBm and ORBl (Van De Werd et al., 2010), as well as MM (Wang et al., 2012), ECT and PERI (Beaudin et al., 2013).

For the 6 remaining PVtdT-expressing parcels, at least one of M2, VGluT2 and CO markers revealed additional subdivisions, indicated by colored labels and dashed lines in Figure 1A, while 7 borders had to be inferred from their stereotypical position relative to PVtdT-labeled landmarks. Such compound parcels were found in retrosplenial (RSPagl, RSPd, RSPv), motor (MOp, MOs), temporal (TEa, TEp), auditory (AUDv, AUDpo, DP, AUDd) and visual extrastriate (one parcel containing AL, LLA, RL, A, AM and PM, and another with LM, LI, P, POR and PORa) cortex, denoted in Figure S1C by red and pink shading. These compound parcels were sub-divided as follows:

*Retrosplenial cortex*, here we observed intensive expression of M2 in its 0.5 mm wide agranular part (RSPagl) and moderate VGluT2 and M2 expression in its ~0.25 mm dorsal part (RSPd).

*Motor cortex*, showed intense, uniform PVtdT expression without an obvious boundary between MOp and MOs (Tanahira et al., 2009) (Figures 1A and S1C). However, a clear border between both motor areas was apparent in the transition from strong to weak CO reactivity (Figures 1D and S1F). On PVtdT maps we therefore marked MOp as 1-2mm-wide curved strip along the medial border of SSp and MOs as a 1mm-wide strip adjoining MOp on the medial side.

*Temporal cortex,* TE, was identified as a U-shaped belt of extremely weak and uniform PVtdT expression at the ventral border of auditory cortex (Figures 1A and S1C), which was further subdivided by VGluT2 into a more darkly labeled anterior half (TEa) and a weakly expressing posterior portion (TEp) (Figures 1C and S1E).

In *auditory cortex*, the primary area (AUDp) was surrounded by a weakly labeled, uniform belt (Figure 1A, orange labels; Figure S1C; pink shading). On the M2 map, the belt was further subdivided into the more darkly labeled AUDv, AUDpo and AUDd and the intensely labeled posterior dorsal auditory area, DP (also known as PD; Kimura et al., 2004) (Figure 1B, orange labels; Figure S1D). On the PVtdT map AUDv and AUDpo were identified as the anterior and posterior half of the weakly-expressing parcel lateral to AUDp (Figures 1A and S1C). DP was identified in the M2 map as a separate rectangular parcel anterior to TEp, lateral to LI, posterior to SSs and posterior to AUDd (Figures 1B and S1D). In the VGluT2 and CO maps DP stood out as a medially-facing nose of a uniformly labeled auditory cortex (Figures 1C, 1D, S1E, and S1F, dark red shading). The overall partitioning of auditory cortex closely resembled the five separate tonotopic maps (Issa et al., 2014; Tsukano et al., 2016).

In *extrastriate visual cortex*, PVtdT expression was more intense in a boot-shaped compound parcel (Figure S1C, red shading) at the lateralposterior side of V1 (Figure 1A, yellow labels), surrounded by ECT, TEp, DP and AL. PVtdT expression in the parcel continuing forward and around the tip to the medial side of V1 (Figure S1C, pink shading) was weaker (Figure 1A, blue labels). Both of these extrastriate visual PVtdT parcels overlapped with similar parcels found in M2 and CO maps (Figures 1B, 1D, S1D, and S1F). Although bipartite by all of these markers, previous topographic mapping of extrastriate visual cortex has shown that the anteromedial parcel contained AL, RL, A, AM and PM, whereas the lateralposterior comprised LM, LI, P, POR and PORa (previously denoted 36p) (Wang and Burkhalter, 2007; Wang et al., 2011). Of all these areas only POR and PORa stood out as a VGluT2-expressing sub-parcel located at the foot of the lateral PVtdT-expressing boot (Figures 1C and S1E, red shading). Furthermore, the toe was more darkly stained with M2 and marked area PORa (Figures 1B and S1D, dark red shading), which was previously known as 36p and identified by its low abundance of the non-phosphorylated intermediate filament protein, SMI32 (Wang et al., 2011). Although PVtdT revealed few details of this organization, labeling in layer 4 provided readily identifiable landmarks (V1, SSp, RSP, AUDp) and unambiguous reference points (tip of V1, barrels of SSp, rhinal fissure [rf], TEp) for accurately positioning all of the extrastriate areas and complete their borders based on the size and shape determined previously by mapping visuotopic connections (Wang and Burkhalter, 2007; Wang et al., 2011). For example in the lateral parcel, POR was centered on the foot of the

PVtdT expressing boot lateral to V1 (> 0.75/ < 1.5 mm lateral/medial of V1 and 0.75 mm anterior to the rf), PORa occupied the toe (> 1.5mm lateral of V1) and P the heel (< 0.75 mm lateral of V1, < 0.6 mm anterior to the rf) (Figure S1C). LM and LI occupied medial and lateral parts of the boot shaft, respectively (LM: < 0.8 mm lateral of V1, > 1.25 mm anterior to POR/P; LI: > 0.8/ < 1.1 mm lateral of V1, < 1.2 mm anterior to POR).

In the weakly PVtdT-expressing parcel around the tip and the medial side of V1, M2- and CO-expression was distinctly sparser (Figures 1A, 1B, and 1D, blue labels; Figures S1C, S1D, and S1F, pink shading). Although uniform by these markers, topographic and callosal mapping has identified six areas, AL, LLA, RL, A, AM and PM within this belt (Garrett et al., 2014; Wang and Burkhalter, 2007), which were not revealed by PVtdT, M2, VGluT2 or CO. Nevertheless, we have annotated these areas based on their stereotypical position relative to PVtdT-labeled landmarks. Specifically, AL was a triangular area with its vertex at the lateral posterior corner of SSp, its base at the border with LM (2 mm anterior to the rf) marked by a sharp decrease in PVtdT expression (Figure 1A; Wang et al., 2011). Of the two remaining sides one was parallel to V1 (1 mm lateral of V1) and the other ran parallel to the lateral border of SSp from its posterolateral corner to intersect V1 at an approximately right angle (Wang and Burkhalter, 2007). LLA was the rectangle enclosed by DP, SSs and AL and a line parallel to the V1 border, intersecting the lateral posterior corner of SSs. RL occupied a 0.7 × 1.2 mm wide rectangle between AL, V1 and SSp with the medial border aligned with the E-row of the barrel field (Figure 1A). Area A was a 0.65 × 0.75 mm wide rhomboid between the tip of V1 and SSp, bordering RL and AM (Figure 1A). AM extended between the tip of V1 to the medial corner of SSp and was bordered laterally by A (Figure 1A). Its medial border was a narrow longitudinal strip of low PVtdT-, M2-, VGluT2- and CO-expression in MM (Figure 1A). The posterior border of AM was a line through the tip of V1 angled backward by 35° from the coronal axis. PM was the triangle behind AM between MM and V1 (Figure 1A). MM was a narrow strip with sparse PVtdT, M2, VGluT2 and CO expressions, which separates PM/AM from the strongly VGluT2-expressing agranular retrosplenial area (RSPagl) (Figures 1A–1D and S1C–S1F).

The accuracy of parcellation was estimated by comparing maps drawn independently by 3 investigators. This involved a zeroing procedure by which stacks of sections were aligned to the pattern of PVtdT expression in layer 4 of V1 and SSp, the borders of 25 uniformly PVtdT-expressing parcels were outlined (Figure 1A), and the parcels were further subdivided into 41 areas based on position relative to readily identifiable PVtdT-positive or -negative landmarks (i.e., tip of V1, SSp, RSP, AUDp, TE, rhinal fissure), shape, and size revealed by previous mapping of connections, expression patterns of M2, VGluT2 and CO (Wang and Burkhalter, 2007; Wang et al., 2011, 2012). The spread in the location of areal borders between visual areas (LM/LI, LM/AL, LM/P, LM/POR, AL/RL, A/AM) measured in 5 animals was 87-142 μm. Our estimate of a < 150 μm-wide transition zone between neighboring areas differs from the sharp borders annotated in the Allen Brain Atlas (ARA; Zingg et al., 2014) and the crisp boundaries derived from averaging of background fluorescence in sections from 1231 mice (Oh et al., 2014). It is important to note that this large sample size reduced the variance over that seen in single cases, suggesting that our maps are not only highly accurate but as shown in Figures S1A and S1B, remarkably similar to those of the Common Coordinate Framework. Thus the important difference to Oh et al. (2014) and Zingg et al. (2014) is not the parcellation per se but the precise registration of DY injection sites and labeled neurons with parcellations derived in each individual case.

## QUANTIFICATION AND STATISTICAL ANALYSIS

### Computation of FLNe

The assignment of the labeled neurons to their respective cortical areas resulting from the parcellation was done with in-house software, written in Python 2.7. The fraction of labeled neurons per area (FLNe) was computed by dividing the number of labeled neurons expressed within the area by the total number of labeled neurons, extrinsic to the injected area, from the ipsilateral cortical hemisphere.

FLNe data is available in Table S6.

### Overdispersion

Quantifying variance of weights (FLNe) allows accurate statistical inferences based on the data and estimation of the uncertainties associated with observed weight values. This allows evaluation of connectivity profiles and provides useful constraints on how well single injections can be used to estimate connectivity profiles (Markov et al., 2011, 2014a).

Count data are intrinsically heteroscedastic, meaning that their variability depends on the mean (Hilbe, 2007). The simplest case occurs when counts are well-described by a Poisson distribution, and the variance equals the mean. It is usually easier to reason in terms of the standard deviation, the square root of the variance, rather than the variance. The standard deviation (SD) of Poisson distributed data increases as the square root of the mean. This implies that the coefficient of determination, defined as the ratio of the SD to the mean, decreases rapidly with increase in the mean. Hence for counts of 100, 1000, 10000, and 100000 neurons, the expected SDs would correspond to 10%, 3%, 1% and 0.3%, respectively, of the means. For the large counts involved in neural projections, such low variability is unlikely. Previous retrograde labeling data have, in fact, demonstrated that cortical connectivity datasets display significant overdispersion (Markov et al., 2011, 2014b; Scannell et al., 2000).

Overdispersion occurs in count data when the variance increases faster than the mean and is displayed in many datasets (Hilbe, 2007). If overdispersion is ignored, then variance is underestimated and statistical tests become anti-conservative, i.e., significance is attributed to differences that are within the normal variation of the dataset. This underlines the importance of

characterizing the mean-variance relations in the data and using appropriate statistical models that incorporate terms that correctly characterize the dispersion of the data.

Overdispersion can be characterized in a variety of ways. Previous retrograde labeling studies in macaque indicate that a negative binomial distribution provides a reasonable description of the data. The negative binomial distribution can be derived as a mixture of a Poisson and a Gamma distribution. In effect, the Poisson mean is no longer considered to be a fixed parameter, but instead follows a Gamma distribution. This yields a 2-parameter distribution that is specified by its mean and a dispersion parameter, $\theta$ (Hilbe, 2007). The variance of the negative binomial distribution is given by $\sigma^2 = \mu + \mu^2/\theta$. As $\theta$ becomes large, the mean-variance relation approaches that of a Poisson distribution. Thus, the Poisson distribution can be seen as a special case of the negative binomial. For $\theta = 1$, the distribution becomes a geometric distribution that is quite overdispersed. Higher values of this parameter signal less overdispersion. Studies in macaque found an overdispersion parameter of about 7-8 (Markov et al., 2011, 2014b). Importantly, while this reflects considerable variation in counts across injections for a given area, the variability was not sufficient to obscure the 5 orders of magnitude range in the projection strengths obtained from a given injection.

Transformation of the raw counts to FLNe changes their statistical distribution. For example, in the case of the Poisson distribution, normalization of counts results in a variable distributed according to binomial law (Chung and AitSahlia, 2006). The relation of the SD to the mean of a binomial distribution is given by: $\sigma = \sqrt{\mu(1-\mu)/n}$, where the mean is now constrained to be a value in the interval (0, 1) and n is the size of the count. Note that this is an inverted U-shaped function of the mean, but on a double-logarithmic plot, the rising portion continues to follow a square-root law and would be expected to have a slope of 0.5. In Figure 3 this is shown by the red curve in each graph. The curve turns down for values greater than 0.5, but no FLNe values this large are observed, so that the initial portion of the curve can be compared with the data. Importantly, the curve provides a poor description of the data, rising less steeply and predicting values of SD that are systematically below those in the data. This leads to rejecting a simple Poisson model of the variability of the data, as is the case in the macaque (Markov et al., 2011, 2014b) and demonstrates evidence of substantial overdispersion.

How much overdispersion is required to model the data was assessed informally by plotting curves for different values of the dispersion parameter and evaluating what value describes the data best. There is no simple expression for relating the normalized counts, i.e., FLNe, to the SD for a negative binomial distribution. We estimated such a curve, however, by simulating samples from a negative binomial distribution with a fixed dispersion and a range of mean values spanning those obtained in the data and then normalizing the counts as if we were computing FLNe. We repeated this simulation many times and obtained an average curve with which to compare the data. For example, the blue curve in each of the plots of Figure 3 is obtained for simulations with the dispersion equal to 1, generating the prediction for a geometric distribution. Importantly, the data points tend to fall systematically below this curve, providing evidence that the data are not as dispersed as a geometric distribution would predict. We rejected the geometric case more formally by fitting a negative binomial model to the data by maximum likelihood under the constraint that the dispersion was equal to 1 and by letting the dispersion be a free parameter. Nested likelihood ratio tests rejected the geometric distribution for the 2 injection sites shown in Figures 3A and 3B in our mouse data (LM: $\chi^2$ (90) = 57.3, p = 3.8 $10^{-14}$; V1: $\chi^2$ ((180) = 76.8, p = 1.9 $10^{-18}$).

Given that the geometric distribution could be rejected, we repeated the simulations as described above for a wide range of dispersion values to estimate the expected relation between SD and mean FLNe as a function of the dispersion. We then compared these curves with the values in Figure 3 and estimated a dispersion value that minimized the error between the simulation and the data, which constitutes the green curves for each plot with the dispersion parameter and the 95% confidence interval (indicated in brackets).

### Accordance with the negative binomial model

In Figures 3E and 3F the error bars are twice the standard errors of the means from repeat injections.

The solid curves are the predicted values for ordered Gaussian variables with the same mean and SD as the dataset. Specifically, we took the means of log (FLNe) represented by white dots and we computed the parameters of the Gaussian that would best fit these points.

To evaluate whether differences between the predicted values and the data were significant, we simulated 10,000 count datasets from a negative binomial distribution with the same means as the data and with the dispersion parameters obtained from the analyses displayed in Figures 3A and 3B. For each dataset, we normalized the counts by the total to obtain simulated FLNe values. From these distributions, we estimated the 2.5% and 97.5% quantiles to obtain a confidence interval (the gray envelopes in Figures 3E and 3F).

### Variability and consistency

In Figures 4D and 4E we addressed specifically if it is possible in the retrograde studies in mouse and macaque to define a threshold above which all projections can be expected to be consistent. For discrete distributions, it is expected that there is a non-zero probability of observing no neurons, even if the projection exists, simply based on sampling variability. The probability of observing such cases would be expected to increase as the mean size of the projection decreased. In fact, the probability distributions predict the expected incidence of such missing connections. For Poisson distributed data, the probability of observing zero neurons is $e^{-\mu}$, where $\mu$ is the mean number of neurons in the projection. For a negative binomial distribution, the probability of observing zero

neurons is $\left(\frac{\theta}{\theta+\mu}\right)^{\theta}$. Deviations from such predictions in the direction of too many observations of zero labeled neurons (leading to zero-inflation) or too few (leading to zero-deflation) constitute evidence against the statistical model used for the data. An alternative is to explain such deviations as evidence that the connections are actually absent in some animals, providing evidence of individual differences in the connectivity pattern. The overdispersion of the count data might be taken as evidence of individual differences in connectivity strength, which could be due to genetic or environmental influences. However, without detailed knowledge of what factor(s) are responsible for the overdispersion, such a hypothesis cannot be confirmed.

Figure 4D displays mouse data from 13 repeat injections in target areas, where the mean number of neurons for a given projection across the multiple injections is plotted as a function of the total number of neurons counted for each injection. Thus, points are individual projections. Those resulting from different injections but for the same target areas are at identical ordinate values, as they all have the same mean and different abscissa values as injections differ only in the total number of neurons labeled in the brain. When no neurons from a given source area were observed in an injection but were observed in at least one other repeat injection, the point is plotted as a white disk but is otherwise colored. We analyzed the distribution of inconsistent projections by determining whether the features log(Mean) and log(Total) could be used to linearly classify the presence and absence of connections. This can be implemented as a logistic regression in which the expected value of the binary variable (Presence/Absence) is predicted by the two features.

Figure 4E displays the same analysis for the 13 repeat injections in macaque.

### Evaluating Akaike Information Criterion

For every group of repeat injections in V1 and LM (Figures 3A and 3B), we modeled the number of labeled cells in the source areas as a function of two explanatory variables: AREA (a factor with a level for each source area) and BRAIN (the individual from which the counts were obtained). We fitted the data with generalized linear models (McCullagh and Nelder, 1989), with a negative binomial family. We chose the link function to be logarithmic and we used the log of the total number of cells counted from each injection as an offset or constant component, added to the model, so that in fact the FLNe was modeled.

The selection of the factors and interactions that best described the data was based on Akaike's Information Criterion (AIC) that evaluates what terms lead to a model with the best predictive power for new data (Akaike, 1974). AIC is defined as minus twice the log likelihood for the best fitting model plus twice the number of parameters estimated in the model. The second term is a penalty for complexity. Including more factors and interactions will improve the fit to the data. The AIC introduces a penalty for additional parameters, so that in comparing several models, lower AIC values correspond to better models in the sense of balancing a trade-off between model complexity (number of parameters) and goodness of fit. We report the difference in AIC (dAIC) between the models with and without the interaction between factors, so a positive value supports the model without an interaction. For example, when AREA is considered as an explanatory variable then it is treated as a factor with as many levels as source areas that contain retrogradely labeled cells from the injections in the target areas. A model fit to the data containing only this factor provides estimates of the average FLNe and its variability for each level of AREA. If, on the other hand, the best model fit to the data requires that the FLNe values be described by the interaction of explanatory variables AREA and BRAIN, i.e., that the values for a particular area vary significantly across individuals, then there is no basis for describing an average profile of connectivity as a signature.

### Overdispersion and connectivity profiles

In Figures 5A and 5C, to illustrate the relationship between the different levels of the statistical modeling, we performed a simulation of the expected experimental results under three different scenarios for the sampling distribution of the data: Poisson, negative binomial with $\theta = 7$, and geometric (i.e., negative binomial with $\theta = 1$). In each case, we first simulated a log-normal distribution of FLNe with mean and standard deviation based on the average mean and standard deviation of the log FLNe values from all of our mouse injections (red, green and blue curves in Figures 5A–5C). Then we simulated 1000 repeats with dispersion specified according to each of the models. The results of these repeats are plotted as gray, semi-transparent points in Figures 5A–5C. Figure 5D shows the SDs of the FLNe in the source areas plotted against the mean FLNe values, from the 1000 simulations, replicating the relation that we observed in Figures 3A and 3B.

We considered 30 hypothetical source areas with fixed mean FLNe spanning 5 orders of magnitude and evenly distributed along an average log-normal curve with the same mean and SD as one of our injections (red, green and blue, respectively, for the three distributions). Each mean FLNe was multiplied by $10^6$ to give the expected mean numbers of neurons in the source areas. These values were used for generating random counts from each of the distributions (Poisson, negative binomial and geometric), as indicated in the insets of Figures 5A–5C. The set of random counts from every simulation were then normalized by their sum to transform them to simulated values of FLNe. This procedure was repeated 1000 times, thus revealing the expected spread of results from 1000 injections under each of the hypotheses.

### Processing Oh et al. (2014) data

The Oh et al. (2014) study reports densities from data derived computationally from mixed injections involving multiple areas, which we call "computed data," but the Supplementary Information from that study provides results obtained from a small number of unmixed injections, which we refer to as "raw data." We calculate the density of the network that we derived from those unmixed

injections and show that it differs markedly from that reported by Oh et al. (2014) for the computed data and that they are much closer to our results in the present study (see Partial Coverage and Global Claims below).

In the study by Oh et al. (2014), the location of injection sites was inferred from a template. With this computational approach 86% of the 469 injection sites in the brain were reported to involve 2-18 different structures. There were 105 injections restricted to isocortex, of which 76% involved 2-9 different structures. The connections labeled by mixed injections were disentangled, and the strengths of connections between individual areas estimated algorithmically using both mixed and injections restricted to single structures (non-mixed injections). For the computed data, the authors derived from 452 out of 469 experiments across the whole brain a full matrix of interareal connections, from which we extracted the ipsilateral cortico-cortical connections. In contrast, the raw data contains connections from 26 injections confined to 14 single areas (non-mixed injections) in the isocortex.

## Network density

The density of a directed graph is given by the ratio $\rho = M/[N(N\text{-}1)]$ between the number of directed edges (links) $M$ of the graph and the maximum possible number of directed links, $N(N\text{-}1)$, where $N$ is the number of nodes in the graph.

The graph density of the full interareal network (FIN, which contains the whole information about the connections between areas) is a fundamental measure of the graph's overall connectedness, extensively used in network science and also in earlier analyses of cortical connectivity (Markov et al., 2013b, 2014a; Sporns and Zwi, 2004). Referring to the weighted connectivity matrix in Figure 7A (for the full FLNe weights data see Table S6), but employing the corresponding binary connectivity matrix, we can infer the density of the FIN (Janson et al., 2000; Markov et al., 2014a; Newman, 2010). Consequently, $M_{FIN}$ will be the product between the average indegrees $< k >_{in}$ and the number of areas $N_{FIN}$. The density of FIN will be the ratio between this number and the total possible connections $N_{FIN}(N_{FIN}-1)$.

Based on an atlas of 47 areas (41 areas with SSp divided into 7 subareas; Figure S1B), the mouse FIN contains $N_{FIN} = 47$ cortical areas that represent the nodes of the $G_{47x47}$ graph. The directed edges of the FIN correspond to directed connections between nodes, with weights given by the fraction of labeled neurons. Our analysis of the FIN makes use of the $G_{19x47}$ directed subgraph of projections within FIN, which reveals all the in-degrees of the injected 19 nodes. It also makes use of the $G_{19x19}$ *edge-complete* subgraph of FIN, corresponding to the connections among just the 19 injected areas. Both $G_{19x47}$ and $G_{19x19}$ subgraphs contain complete information about the status of their edges and their statistical properties would not be expected to be influenced by injections into additional areas elsewhere in the cortex (see Partial Coverage and Global Claims below). Given that the 19 injected areas are widely distributed across the cortex (Figures S1B and S5), the $G_{19x19}$ subgraph is likely to reflect major characteristics of the FIN.

We performed a dominating set analysis on $G_{19x47}$ (Table S2) for further evidence that the FIN is indeed dense (Figure S4B). In graph theory, a subset $D$ of nodes of a graph $G$ with node set $V$ is said to be dominating $G$, if all elements of $V$ have a link to at least one node in $D$ (Kulli and Sigarkanti, 1991). Here we modify this definition slightly by saying that *D dominates x% of the nodes of G*, if an *x*% of *all* nodes in $V$ are linked to one or more nodes in $D$. The $x\% = 100\%$ corresponds to "full" domination. This definition includes also nodes from $D$. The Minimum Dominating Set (MDS) $D_{min}$ is defined as the one that fully dominates $G$ and it has the smallest size (number of nodes).

## Partial coverage and global claims

For the following analysis, for simplification, we'll name ABI the data from Oh et al. (2014) and SBRI (Stem cell and Brain Research Institute) the data obtained in the present study.

Density calculation: The density of square 1-0 matrices NxN is calculated the standard way by dividing the number of 1-entries with the number of matrix elements minus the number of intrinsic connections (A→A type entries), i.e., by N(N-1). The density of rectangular 1-0 matrices NxM with N denoting the number of injected areas and N < M, is calculated by dividing the number of 1-entries by the number of matrix elements less the number of intrinsic connections, i.e., by NM-N.

Dataset #1: The ABI anterograde (Oh et al., 2014) raw data is based on anterograde injections in 14 areas and identifies labels in a 40-area atlas. Accordingly, the 14x14 edge-complete square matrix/graph has a density of 90.11% and the 14x40 matrix has a density of 92.12%.

Dataset #2, ABI parcellation: For our retrograde data with the Oh et al., 2014 (ABI) parcellation, the matrix is 21x45 (Figure S6A), with a density of 95.71% for the 21x21 edge-complete (injected) subgraph (Figure S6B), and a density of 96.1% for the 21x45 matrix.

Dataset #3, present parcellation: For our retrograde SBRI data with our present parcellation, the matrix is 19x47 (Figure 7A), with a density of 97.37% for the edge-complete 19x19 matrix (Figure 7A) and the same density of 97.37% for the full 19x47 matrix.

This shows that across different parcellations and different datasets from different experiments, and different methods (anterograde versus retrograde), the mouse matrix connectivity density is consistently above 90%.

The connectome is not uniform; as shown previously, both in the macaque and mouse, the connectome is organized into a core-periphery structure with the cortical network core (primarily of high degree nodes) mostly comprised of associative areas. Selecting target areas only from the core, would, indeed generate an edge-complete subgraph that is very dense. However, all datasets include both primary and associative injected areas. In particular, ABI injected 6 primary areas, representing 43% of the 14 injected areas. SBRI with ABI parcellation has 5 primary areas injected, representing 24% of the 21 areas injected, while SBRI with present parcellation has the same 5 primary areas injected, which forms 26% of all injected areas. Additionally, the choices of the locations of injections between the two sets of experiments (ABI and SBRI) differ considerably. As we have shown above, all densities are consistently above 90%.

Next, we investigate the possibility that the non-injected areas contribute only with a low connectivity so that the full graph would have a lower final density. Recall that retrograde tract tracing reveals all the incoming connections to the injected node, from both

injected and non-injected nodes. If the non-injected nodes contributed a lower connectivity to the connectome, then we should observe lower out-degrees from the non-injected nodes to the injected set, when compared to the out-degrees of the injected nodes to injected set. Table S4 shows the values of the out degrees for nodes separated into the injected and non-injected groups respectively. To be able to compare similar quantities, we normalize by the number of injected nodes. For example, for our data with the ABI parcellation, there are 21 injected nodes, but an injected node can send out-links only to 20 other nodes from the injected set (no out-links to self), whereas a non-injected node can send outlinks in principle to all the 21 injected. Thus, if we divide the outdegree of an injected node by their number minus one (20) and the outdegree of a non-injected node by 21, we get the fraction of injected nodes toward which a specific node has an outlink to. We then repeat this with the SBRI data and present parcellation (with 19 injected nodes), shown in Table S5. For the ABI parcellation (Table S4), the outlink average fraction for an injected node is 95.7%, with a standard deviation of 5.7%, whereas for a non-injected node the same quantity is 96.4% with a standard deviation of 7.3%. Thus, from an out-degree point of view, toward the same set of nodes, there is virtually no difference between an injected node or a non-injected node. For the SBRI dataset with the present parcellation (Table S5), the average out-degree fraction of an injected node is 97.4% with a standard deviation of 3.9%, whereas the same quantity for non-injected nodes is an average of 97.4% and standard deviation of 4.4%.

For anterograde tract tracing, the roles of out-links and in-links are reversed, as in this case all the outlinks are revealed for an injected area. Repeating the same analysis as above with the anterograde ABI (raw) data, we find a similar pattern, as shown in Table S3. The average in-degree fraction of an injected node is 90.1% with a standard deviation of 8.8%, whereas the same quantity for non-injected nodes is an average of 93.1% and standard deviation of 8.7%. Here as well, from an in-degree point of view, we see no significant difference between an injected node or a non-injected node.

The above data all show very similar numbers with small deviations and they indicate that there is nothing special in terms of out-degrees between injected and non-injected nodes, and across different parcellations.

### In-degree analysis for retrograde data

Since retrograde injection in an area reveals all its incoming connections, the in-degrees into the injected areas will not change with additional injections, they are final. Figures S8A and S8B show the in-degree distribution for the SBRI dataset for both parcellations (ABI and present). In both cases the in-degrees are very high, near the maximum. For the Oh et al. (2014) parcellation (21x45 matrix), among the 21 injected areas, 10 receive in-links from all the rest (45-1 = 44), five from 43, two from 42 and the lowest is one area receiving in-links from 33 others. More than 85% of the nodes, each, receive at least 93% of all possible incoming connections. For the present parcellation (19x47 matrix), among the 19 areas 13 receive from maximum possible (46) one from 45, two from 44 and the lowest receives 38 in-links. More than 84% of the nodes, each, receive at least 95% of all possible incoming connections! Clearly, other injections would bring new edges into the network. Assuming that the average in-degree of the non-injected nodes is the lowest value found among the injected nodes (although the previous analysis shows that it should be higher than this assumption), even this brings the full network density down to only (33x24+888)/(45x44) = 85% for the ABI parcellation and to (38x28+851)/(47x46) = 89% for the SBRI parcellation, both still very high.

### Network communication efficiency

The five order of magnitude variability in the interareal projection weights indicates strong specificity, and has important consequences, in particular on the capacity, or bandwidth of information transfer between cortical areas. This is best illustrated via network communication efficiency measures, first introduced in network science applications by Latora and Marchiori (2003) and expanded upon by Vragović et al. (2005). There are two such measures, the global efficiency measure $E_g$ (Latora and Marchiori, 2003) and the local efficiency $E_l$ (Vragović et al., 2005). $E_g$ is the average conductance between all source-target pairs in the network, whereas $E_l$ measures the conductance between the neighbors of an area X through the network that does not include X, averaged over all neighbor pairs and for all X. Conductance from a source node to a target node is a weighted measure and it's given by the conductance of the path of minimal total resistance through the network from source to target. As explained in Markov et al. (2013b), resistance for information transfer along a projection can be modeled as the negative logarithm of the FLN edge weight of that projection and therefore resistances are additive along paths. Accordingly, a directed path from source to target that contains only high FLN edges will have a very low resistance and thus high conductance, or high information transfer bandwidth and vice-versa. In Ercsey-Ravasz et al. (2013) and Markov et al. (2013b), both the global and local efficiency measures revealed an optimal organization for information transfer in macaque cortex. The same studies showed that this optimal organization was well captured by the exponential distance rule (EDR) model, which describes the negative exponential dependence of weights on distance.

The clustering analysis and plotting from Figures 8D–8G was done with Pajek, and it uses the Kamada-Kawai force-based algorithm (Kamada and Kawai, 1989), which draws areas that share stronger connections closer to one another than otherwise.

## DATA AND SOFTWARE AVAILABILITY

The FLNe data is available at http://.core-nets.org/.

Requests for additional data and software should be directed to the Lead Contact, Henry Kennedy (henry.kennedy@inserm.fr) and to the Corresponding Author, Andreas Burkhalter (burkhala@wustl.edu), and will be made available upon reasonable request.

**Neuron, Volume *97***

## Supplemental Information

# The Mouse Cortical Connectome, Characterized by an Ultra-Dense Cortical Graph, Maintains Specificity by Distinct Connectivity Profiles

**Răzvan Gămănuţ, Henry Kennedy, Zoltán Toroczkai, Mária Ercsey-Ravasz, David C. Van Essen, Kenneth Knoblauch, and Andreas Burkhalter**

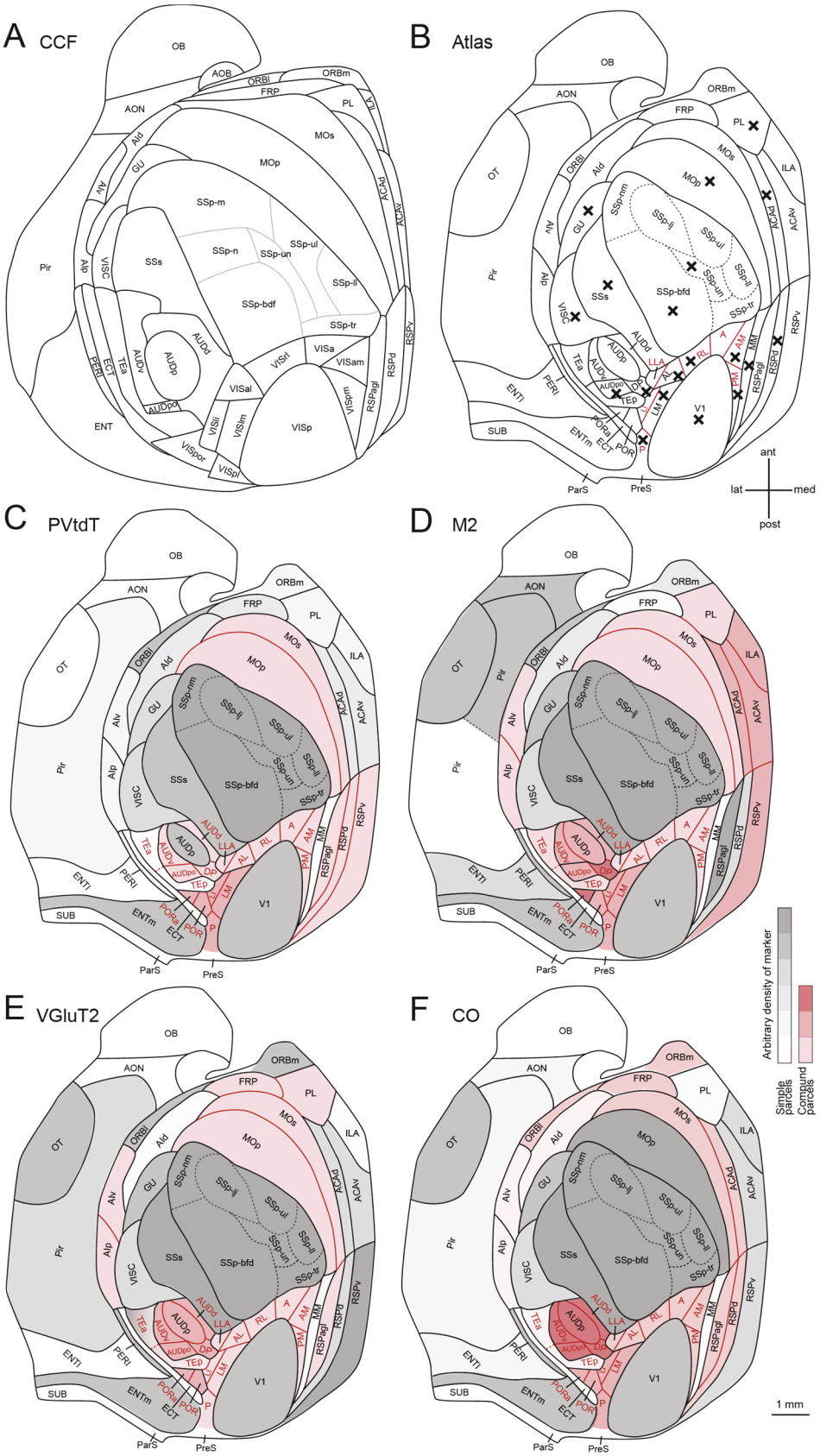


**Figure S1. Partitioning schemes revealed by different markers expressed in tangential sections through layer 3-5 of flatmounted left mouse cerebral cortex (Related to Figure 1)**

(**A**) Flatmap showing areal borders observed in average background fluorescence intensity imaged by serial two-photon tomography. Adapted from version 3 of the Allen Mouse Common

Coordinate Framework (CCF) (brain-map.org). (**B**) Atlas of 41 areas used in this study, derived from a combination of PVtdT, M2, VGluT2 and CO expression. Positively identified areas are delineated with black lines and denoted in black letters. Red lines and letters indicate borders and areas, known from topographic mapping (Garrett et al., 2014; Wang and Burkhalter, 2007) or identified by location relative to landmarks observed in the PVtdT map. Black crosses indicate the 19 DY-injected areas. Note that SSp is injected into subareas SSp-bfd and SSp-un. (**C**) Parcellation scheme based on the expression of PVtdT. Black solid contour lines delineate positively identified 'simple parcels' (i.e. which could not be further subdivided) based on intensity of PVtdT expression (arbitrary shades of gray). PVtdT expression in the red-shaded 'compound parcels' (i.e. which contained additional sub-parcels) was uniform and revealed no detectable borders (red lines) between presumptive areas. Note that PVtdT expression in lateral extrastriate visual cortex was more intense (dark red) posterior to the LM/LI-AL border, marking a parcel that contained P, POR, PORa, LI and LM. TE stood out by undetectable PVtdT expression, which failed to reveal a border between TEa, TEp and ECT. Dashed black lines denote subareas within SSp, representing different body parts. (**D**) Parcellation scheme based on M2-expression. Black solid contour lines delineate positively identified parcels denoted in black letters. M2 expression in red-colored parcels was relatively uniform, but differed in intensity between parcels (note different shading) this allowed the detection of borders between parcels (black lines) but not within parcels (red lines). Names indicate presumptive areas, which could not be positively identified. (**E**) Parcellation scheme based on VGluT2 expression. All conventions are the same as in (B-D). (**F**) Parcellation scheme based on cytochrome oxidase reactivity (CO). All conventions are the same as in (C-E).

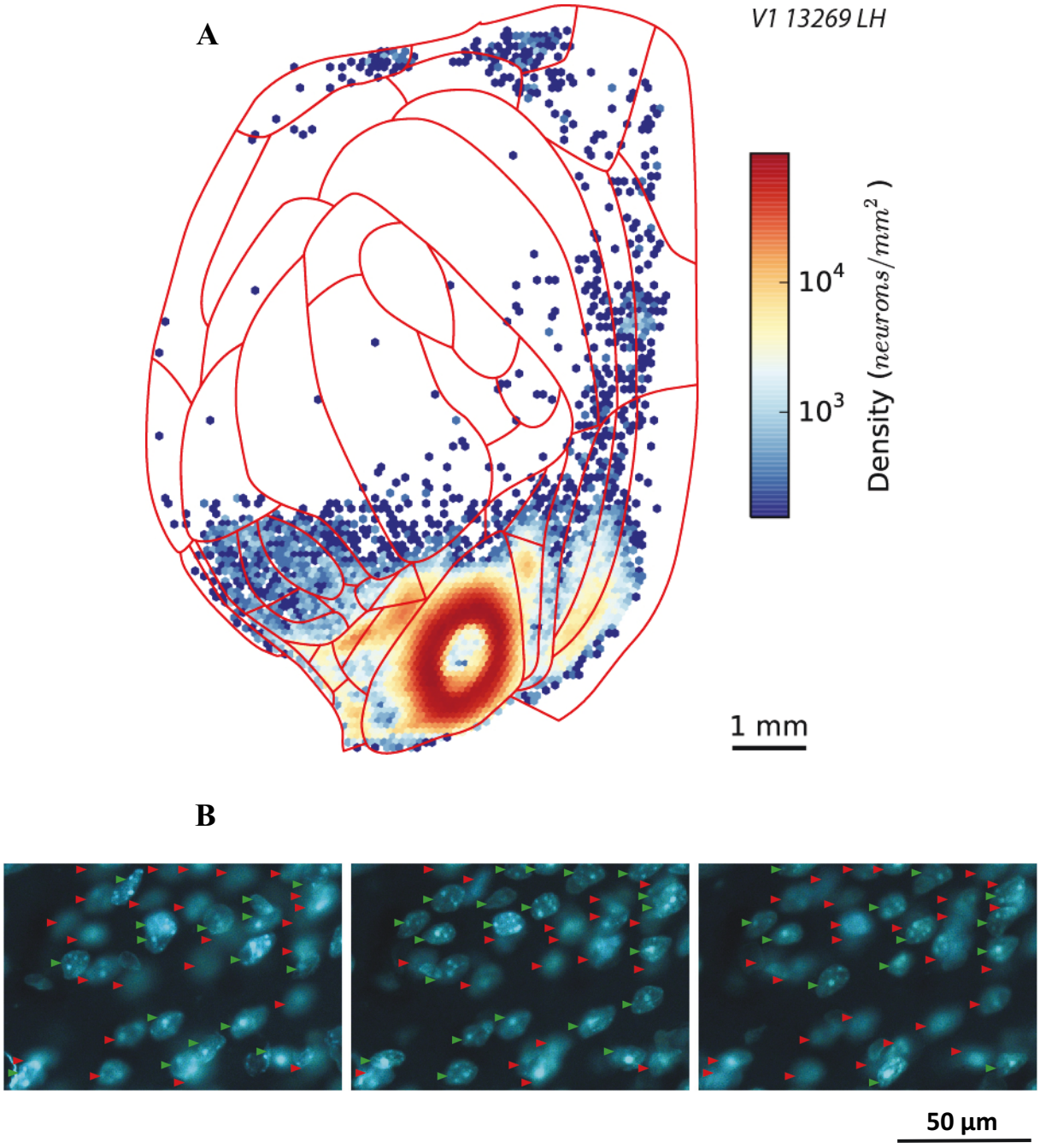


**Figure S2. Charting the labeled neurons (Related to Figure 2)**

**(A)** Single-neurons are clustered to show how density varies with respect to areal borders. **(B) S**ingle microscope field imaged at three different focal depths. Each labeled neuron is tagged with a red or green triangle. Red triangles, labeled neurons that are not in the focal plane; green triangles, labeled neurons in the focal plane. This figure illustrates that extensive use has to be made of the Z-axis to accurately identify labeled neurons.

**Parcellation adapted to resemble as close as possible the one used by Oh et al. (2014)**

**Oh et al. (2014)**

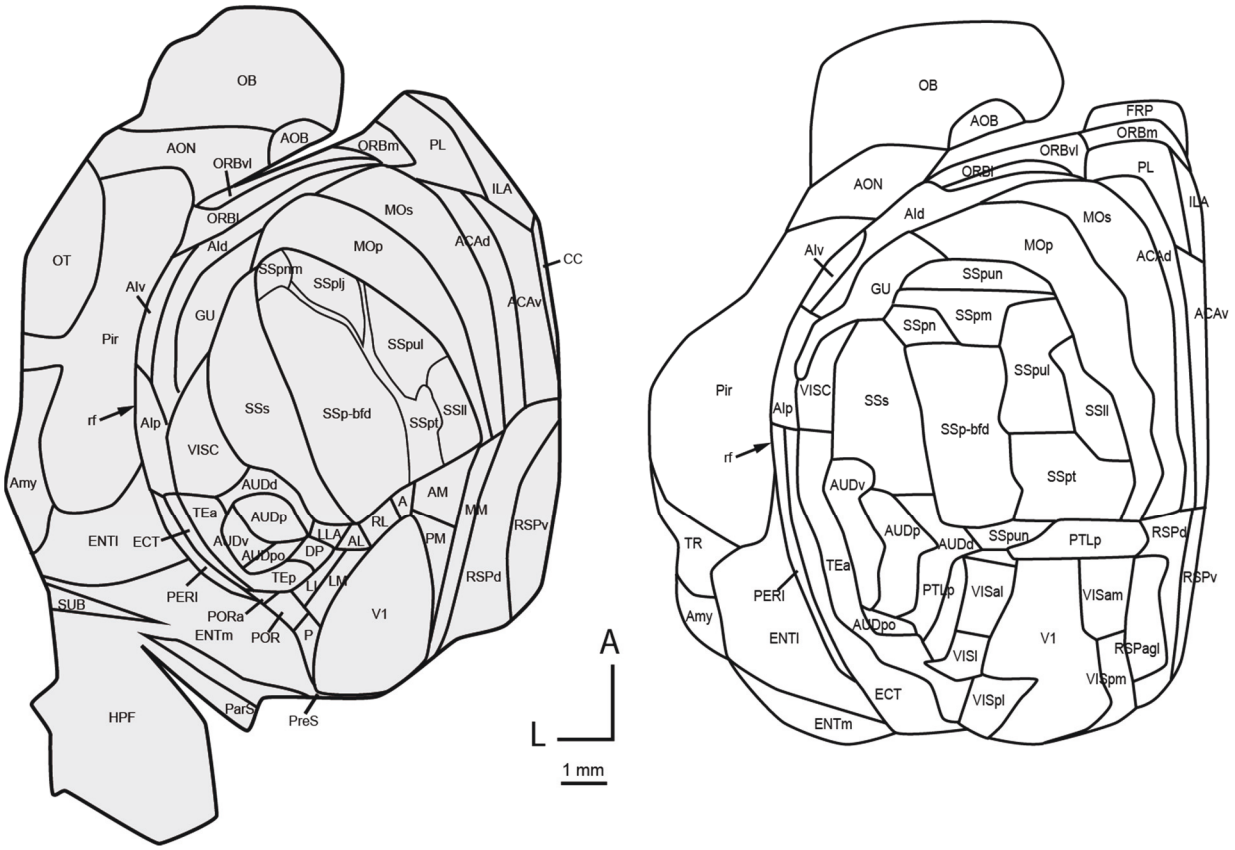


**Figure S3. Atlases allowing comparisons of present labeling with that of the Oh et al. (2014). (Related to Figure 6 and** *Partial coverage and global claims* **in STAR Methods)**

Left, a parcellation of the present material adapted to resemble that used by Oh et al. (2014). This parcellation is used in **Figure 6**, as well as to support the claim that changes in the parcellation do not change the density significantly (*Partial coverage and global claims* in **STAR Methods**). Right, parcellation used by Oh et al. (2014) adapted to the flattened brain.

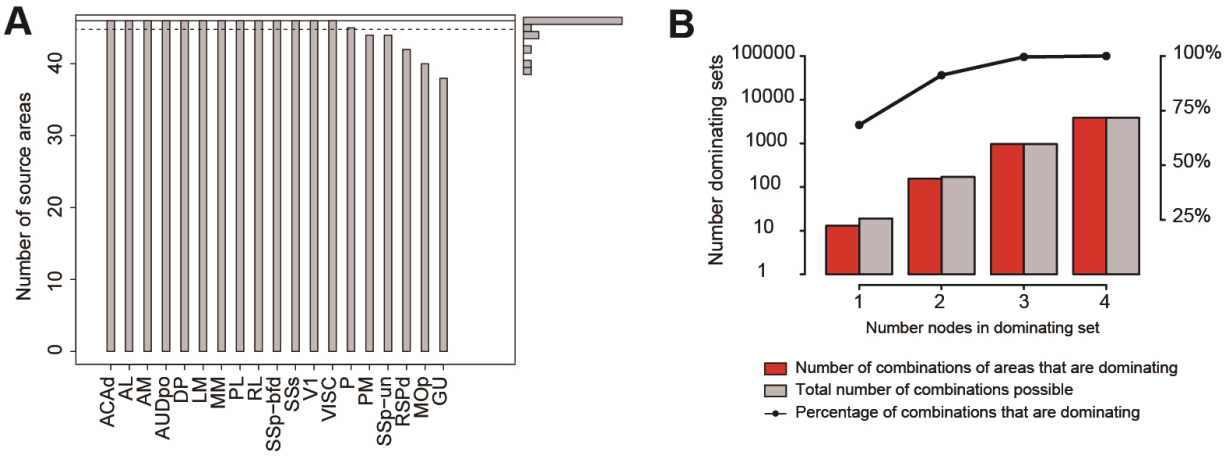


**Figure S4. Analysis of in-degree distribution and dominating sets (Related to Figure 7)**

(**A**) In-degree sequence (big graph), with the in-degree distribution of injected areas (small barplot on right y-axis). (**B**) Red bars, number of subgraphs that dominate 100% the $G_{19x47}$. Gray bars, total possible number of subgraphs corresponding to the red bars. The ratios of the two sets, expressed in percentages, is shown by the black dots, which have the y axis on the right.

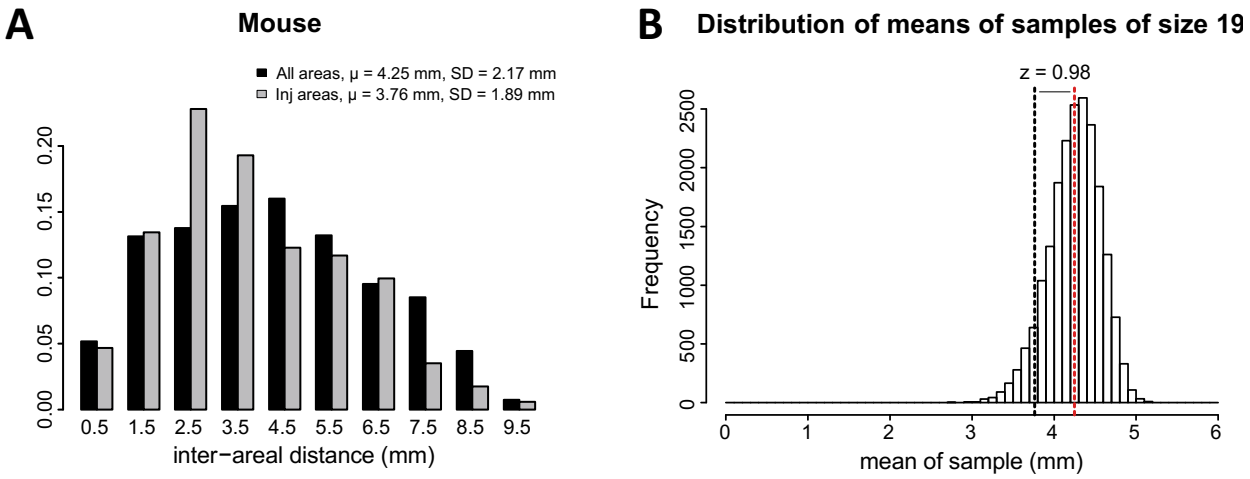


**Figure S5. Spatial coverage of injections across the cortex (Related to Figure 1,** *Network density* **in STAR Methods and Figure S1)**

**(A)** Comparison in mouse of the distances between all cortical areas (black) and those between injected areas (gray). The two means are not far from each other and there is no strong skewness for the distances between injected areas, suggesting that this set of areas comes close to a random sample. (**B)** The mean of distances between the injected areas is statistically indistinguishable from the mean of distances between all areas. The white bars form the distribution of means of 20, 000 random samples of size 19, without replacement, from the set of 47 areas. The z score of the mean distance between the injected areas (black dashed line) is 0.98, less than one standard error from the mean of all distances (red dashed line). This gives a p-value of 0.32 for the two-sided test, which demonstrates that the two are not statistically different.

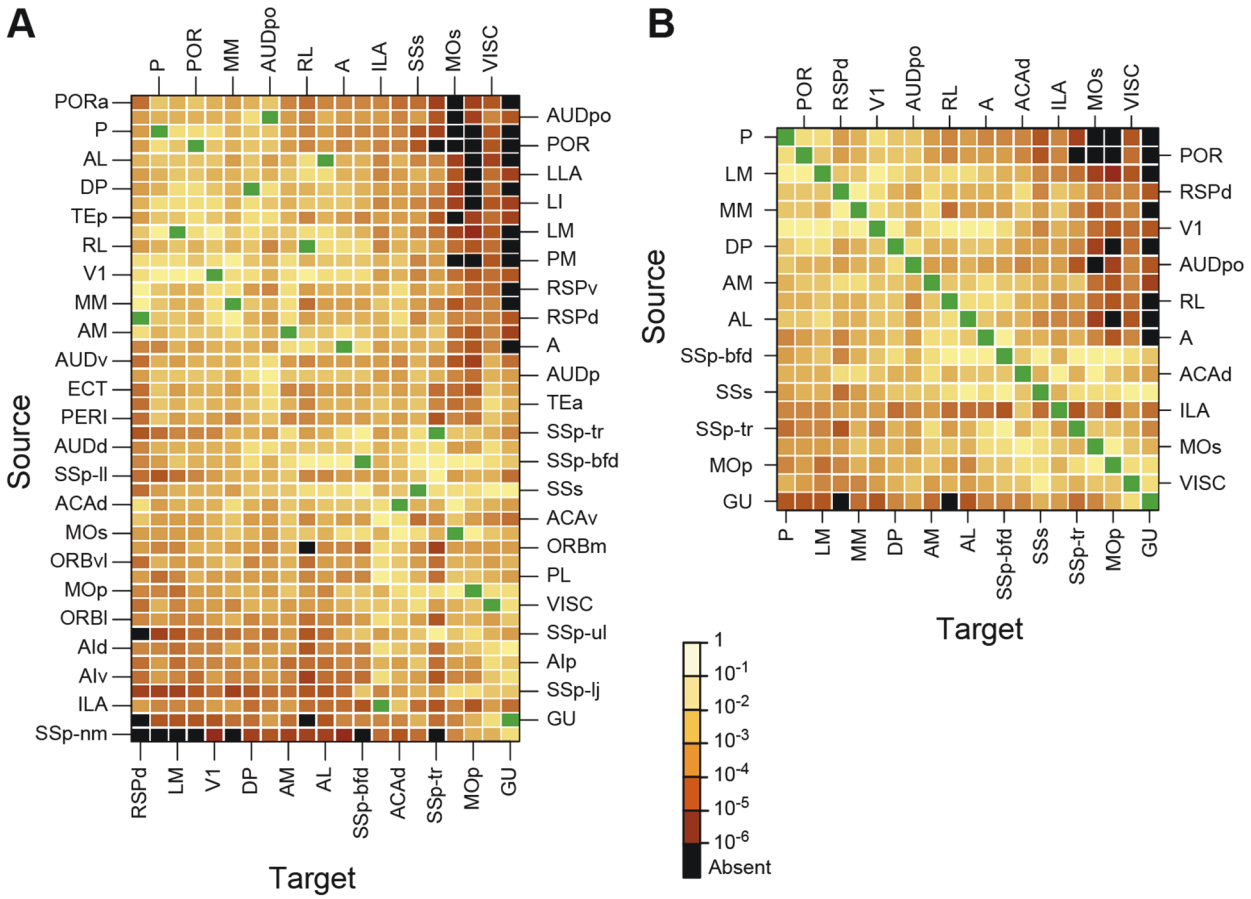


**Figure S6. Weighted connectivity matrix generated with FLNe data from the present study using parcellation of the Oh et al. (2014) study (Related to Figure 7)**
Strength of the projection (FLNe) are color coded; black, absent connections; green, intrinsic projections where FLNe is not indicated. (**A**) Rows, one of the 45 source areas; column, one of the 19 injected target areas. Note that the SSp-bfd and SSp-un subfields are listed as separate areas. The row and column ordering was determined by a clustering algorithm based on input and output profile similarity. (**B**) A weighted connectivity matrix for the 19x19 subgraph. For multiple injections, FLNe indicates the arithmetic mean.

Comparison of this figure with **Figure 7** of the main text shows many similarities in the connectivity matrix composed with the parcellation of the present study or that of the Oh et al. (2014) study.

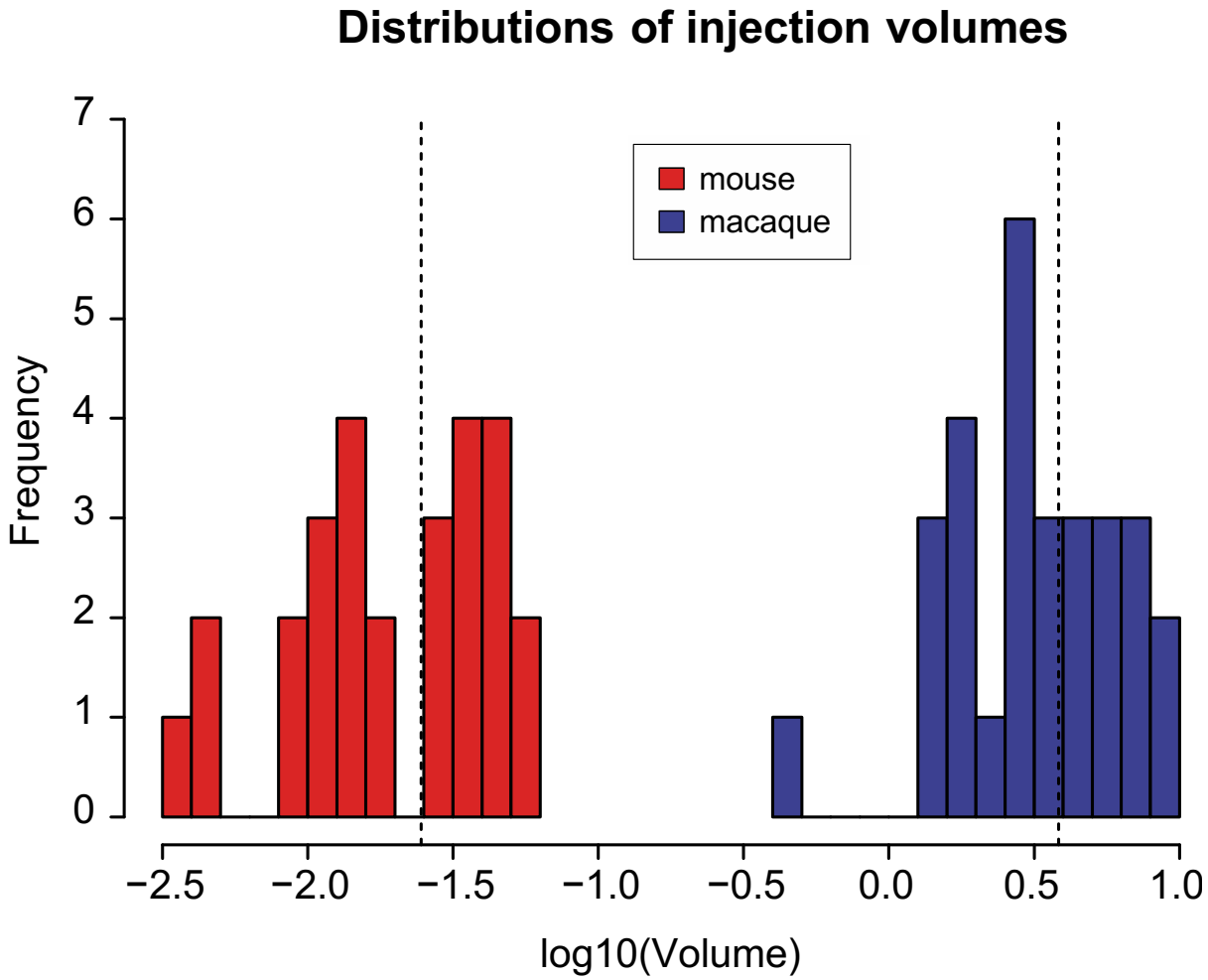


**Figure S7 Distributions of volumes ($mm^3$) of uptake zones for mouse (red, current study) and macaque (blue, Markov et al. [2011]), on a logarithmic scale (Related to Figure 2)**

The vertical dashed lines are the averages of each distribution. Notice that there are more than two log units between the two, meaning that injections in macaque are more than 100 times bigger on average than in mouse, which follows the increase in the volume of the cortex. The flattened mouse neocortex has a surface of little less than 100 $mm^2$ (current measurements), while the flattened macaque neocortex has about 10 000 $mm^2$ (Sincich et al., 2003). It is known that the width of the cortex varies very slowly with increase in brain size (Stevens, 1989), therefore the width contributes very little at the difference in volumes. The result is a two fold increase in the volume of the macaque neocortex with respect to mouse, the same as for the volumes of injections. Therefore, the ratio between the injection volume and the volume of the cortex stays largely constant and we can consider the experiments equivalent in the two species.

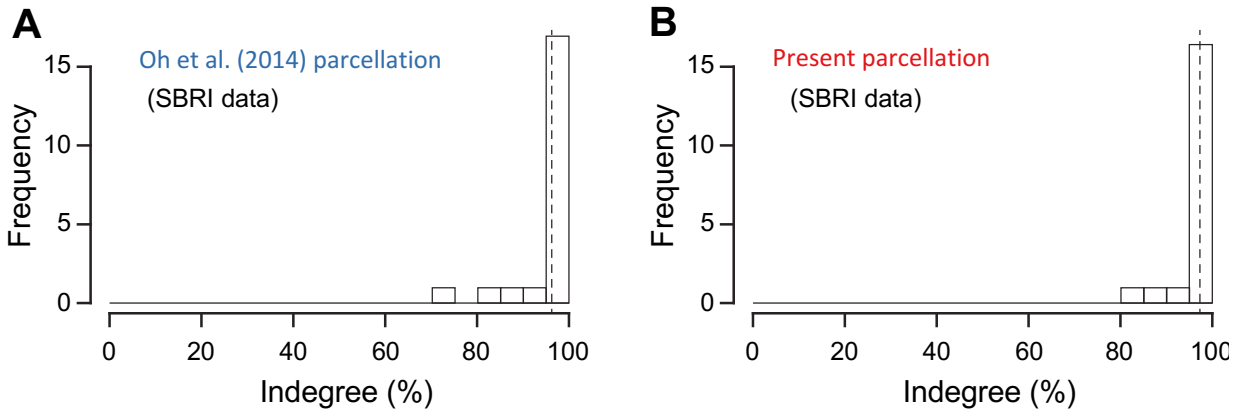


**Figure S8. In-degree distributions (Related to Figure 7 and** *In-degree analysis for retrograde data* **in STAR Methods)**

(**A, B**). In-degree distributions for retrograde tracing data in the present study using different parcellations. The in-degree on the x axis is expressed as a percentage of the maximum possible degree: **(A)** for the ABI parcellation it is 44 and **(B)** for the present is 46. Vertical dashed lines represent the mean values.

**Table S1 Weights of cortical labeling in Oh et al. (2014) following injections in pontine nucleus, superior colliculus and basal ganglia (Related to Figure 6I)**

Raw Data

| | | | | | ISOCORTEX | | | | | | | | | | | | | | | | |
|---|---|---|---|---|---|---|---|---|---|---|---|---|---|---|---|---|---|---|---|---|---|
| image-series-id | specimen-name | primary-injection-structure | secondary-injection-structures | injection volume (mm^3) | FRP | MOp | MOs | SSp-n | SSp-bfd | SSp-ll | SSp-m | SSp-ul | SSp-tr | SSp-un | SSs | GU | VISC | AUDd | AUDp | AUDpo | AUDv | VISal | VISam | VISl |
| 100142580 | 378-824 | Caudoputamen (CP) | | 0,085084188 | 0,00127526 | 0,000503595 | 0,00383692 | 0,000528003 | 0,00144933 | 0 | 0,000335368 | 0,000352128 | 0 | 0 | 0,00199202 | 0,00041749 | 0 | 0 | 0,000423471 | 0 | 0 | 0 | 0 | 0 |
| 112307754 | 378-931 | Caudoputamen (CP) | | 0,1045426 | 0 | 0,0138555 | 0,0125699 | 0,000847282 | 0,0538486 | 0,00465863 | 0,000794236 | 0,0330389 | 0,0532484 | 0,000985946 | 0,00471056 | 0,00111423 | 0,000437193 | 0,00521289 | 0,00436139 | 0 | 0,00834458 | 0,000833825 | 0 | 0 |
| 112458831 | 378-962 | Caudoputamen (CP) | | 0,080538097 | 0,00134468 | 0,0355772 | 0,0537975 | 0,000483111 | 0,0127749 | 0,0119877 | 0,0020463 | 0,00168645 | 0,00102551 | 0,00305528 | 0,00680754 | 0,00228708 | 0,000754743 | 0,000931177 | 0,00114052 | 0 | 0,00125435 | 0 | 0,000939198 | 0 |
| 127255254 | 378-1292 | Nucleus accumbens (ACB) | | 0,090176233 | 0 | 0,000503595 | 0,00383692 | 0,000528003 | 0,00144933 | 0 | 0,000335368 | 0,000352128 | 0 | 0 | 0,00199202 | 0,00041749 | 0 | 0 | 0,000423471 | 0 | 0 | 0 | 0 | 0 |
| 272917631 | 378-1883 | Lateral septal nucleus (LS) | | 0,068583257 | 0 | 0 | 0,0386105 | 0 | 0,00216066 | 0 | 0 | 0 | 0 | 0 | 0,00189567 | 0,000400633 | 0 | 0 | 0 | 0 | 0 | 0 | 0 | 0 |
| 112827164 | 378-1071 | Superior colliculus sensory (SCs) | SCm | 0,050616994 | 0 | 0,0012334 | 0,00172016 | 0,00150936 | 0,0082655 | 0 | 0,00614061 | 0,00200369 | 0,000329847 | 0,00258415 | 0,0181737 | 0,0013985 | 0,00200896 | 0 | 0,000898533 | 0 | 0,000431339 | 0 | 0 | 0 |
| 126646502 | 378-1285 | Superior colliculus motor (SCm) | SCs | 0,246750378 | 0 | 0 | 0 | 0 | 0 | 0 | 0 | 0 | 0 | 0,00119541 | 0 | 0 | 0 | 0 | 0 | 0 | 0 | 0 | 0 | 0,00127055 |
| 152995635 | 378-1579 | Pontine reticular nucleus (PRNr) | | 0,007105834 | 0,00231736 | 0,0690465 | 0,0345537 | 0,000805553 | 0,0624673 | 0,00528963 | 0,00187069 | 0,0166336 | 0,0032152 | 0,00586405 | 0,0794251 | 0,026267 | 0,0156547 | 0,00168575 | 0,00884681 | 0,0015789 | 0,0131545 | 0 | 0,0013132 | 0 |

Computed Data

| | Isocortex | | | | | | | | | | | | | | | | | | | | |
|---|---|---|---|---|---|---|---|---|---|---|---|---|---|---|---|---|---|---|---|---|---|
| | ACAd | ACAv | AId | AIp | AIv | AUDd | AUDp | AUDv | ECT | FRP | GU | ILA | MOp | MOs | ORBl | ORBm | ORBvl | PERI | PL | PTLp | RSPagl | RSPd | RSPv | SSp-bfd |
| ACB | 0 | 0 | 0 | 0 | 0,009048853 | 0 | 0 | 0 | 0 | 0 | 0 | 0,011187649 | 0,002927303 | 0,003885731 | 0 | 0,016581259 | 0 | 0 | 0,00137311 | 0 | 0 | 0 | 0 | 0 |
| CP | 0 | 0 | 0,009178084 | 0,068206782 | 0 | 0 | 0,001554416 | 0 | 0 | 0 | 0,02561963 | 0 | 0 | 0 | 0 | 0 | 0 | 0 | 0 | 0 | 0 | 0 | 0 | 0 |
| LS | 0 | 0 | 0,000477062 | 0 | 0,000906904 | 0 | 0 | 0 | 0 | 0 | 0 | 0 | 0 | 0 | 0,001357445 | 0,014484476 | 0 | 0,000535786 | 0 | 0 | 0 | 0 | 0 | 0,000203737 |
| SCm | 0 | 0 | 0 | 0 | 0 | 0 | 0 | 0 | 0 | 0 | 0 | 0 | 0 | 0 | 0 | 0 | 0 | 0 | 0 | 0 | 0 | 0 | 0 | 0 |
| SCs | 0 | 0 | 0 | 0 | 0 | 0 | 0 | 0 | 0 | 0 | 0 | 0 | 0 | 0 | 0 | 0 | 0 | 0 | 0 | 0 | 0 | 0 | 0 | 0 |
| PRNr | 0 | 0 | 0 | 0 | 0 | 0 | 0 | 0 | 0 | 0 | 0 | 0 | 0 | 0 | 6,19102E-05 | 0 | 0 | 0 | 0 | 0 | 0 | 0 | 0 | 0,000148034 |

Raw Data

| | | | | | ISOCORTEX | | | | | | | | | | | | | | | | | | |
|---|---|---|---|---|---|---|---|---|---|---|---|---|---|---|---|---|---|---|---|---|---|---|---|
| image-series-id | specimen-name | primary-injection-structure | secondary-injection-structures | injection volume (mm^3) | VISp | VISpl | VISpm | ACAd | ACAv | PL | ILA | ORBl | ORBm | ORBvl | AId | AIp | AIv | RSPagl | RSPd | RSPv | PTLp | TEa | PERI | ECT |
| 100142580 | 378-824 | Caudoputamen (CP) | | 0,085084188 | 0 | 0 | 0 | 0,00211072 | 0,00192592 | 0 | 0,00171659 | 0 | 0 | 0,000664638 | 0,000453821 | 0 | 0,000370864 | 0 | 0,00122094 | 0,000950514 | 0 | 0,000785599 | 0 | 0,000975304 |
| 112307754 | 378-931 | Caudoputamen (CP) | | 0,1045426 | 0,00115925 | 0 | 0 | 0,00392942 | 0,000535188 | 0,00193402 | 0 | 0,00103934 | 0,000431478 | 0 | 0,00123998 | 0,000425783 | 0,000598723 | 0 | 0,000783414 | 0 | 0,00198714 | 0,0116743 | 0,00211835 | 0,00507643 |
| 112458831 | 378-962 | Caudoputamen (CP) | | 0,080538097 | 0,00219828 | 0 | 0,00171559 | 0,0292216 | 0,0394707 | 0,00990807 | 0,00390229 | 0,00624332 | 0,000913278 | 0,0116665 | 0,00157906 | 0,000826815 | 0,0015563 | 0 | 0,00354012 | 0,00352136 | 0,00125042 | 0,00146875 | 0,000573271 | 0,00130182 |
| 127255254 | 378-1292 | Nucleus accumbens (ACB) | | 0,090176233 | 0 | 0 | 0 | 0,00211072 | 0,00192592 | 0 | 0,00171659 | 0 | 0 | 0,000664638 | 0,000453821 | 0 | 0,000370864 | 0 | 0,00122094 | 0,000950514 | 0 | 0,000785599 | 0 | 0,000975304 |
| 272917631 | 378-1883 | Lateral septal nucleus (LS) | | 0,068583257 | 0,00036321 | 0 | 0 | 0,00244548 | 0,0139422 | 0 | 0,000630129 | 0 | 0 | 0 | 0 | 0 | 0 | 0 | 0,000424096 | 0,000917427 | 0 | 0 | 0 | 0 |
| 112827164 | 378-1071 | Superior colliculus sensory (SCs) | SCm | 0,050616994 | 0,00032723 | 0 | 0 | 0,00071930 | 0,00580215 | 0 | 0,00151113 | 0 | 0 | 0,00110777 | 0,00262209 | 0,000646187 | 0,0028012 | 0 | 0,007847 | 0,0821071 | 0 | 0,000608526 | 0,0009246 | 0,00077626 |
| 126646502 | 378-1285 | Superior colliculus motor (SCm) | SCs | 0,246750378 | 0,00128854 | 0,000512247 | 0,00151457 | 0,00032857 | 0,000638905 | 0 | 0 | 0 | 0 | 0 | 0 | 0 | 0 | 0 | 0,0446402 | 0,106554 | 0,000420818 | 0,000745227 | 0 | 0 |
| 152995635 | 378-1579 | Pontine reticular nucleus (PRNr) | | 0,007105834 | 0,00661345 | 0,00152444 | 0,00364719 | 0,00532867 | 0,02144 | 0 | 0,00690107 | 0 | 0,000889636 | 0,00360121 | 0,0246485 | 0,0159319 | 0,0168589 | 0,00184076 | 0,123002 | 0,107153 | 0,0027982 | 0,0265975 | 0,0337612 | 0,038383 |

Computed Data

| | Isocortex | | | | | | | | | | | | | | | |
|---|---|---|---|---|---|---|---|---|---|---|---|---|---|---|---|---|
| | ACAd | ACAv | AId | AIp | SSp-ll | SSp-m | SSp-n | SSp-tr | SSp-ul | SSs | TEa | VISC | VISal | VISam | VISl | VISp | VISpl | VISpm |
| ACB | 0 | 0 | 0 | 0 | 0 | 0 | 0 | 0 | 0 | 0 | 0 | 0 | 0 | 0 | 0 | 0 | 0 | 0 |
| CP | 0 | 0 | 0,009178084 | 0,068206782 | 0 | 0 | 0 | 0 | 0 | 0 | 0,01312712 | 0,063223559 | 0 | 0 | 0 | 0 | 0 | 0 |
| LS | 0 | 0 | 0,000477062 | 0 | 0 | 0 | 0 | 0 | 0 | 0,00169977 | 0 | 0 | 0 | 0 | 0 | 0 | 0 | 0 |
| SCm | 0 | 0 | 0 | 0 | 0 | 0,000188504 | 0 | 0 | 0 | 0 | 0 | 0 | 0 | 0,00176801 | 0 | 0 | 0 | 0 |
| SCs | 0 | 0 | 0 | 0 | 0 | 0 | 5,08018E-05 | 0 | 2,06238E-05 | 0,000231227 | 0 | 0 | 0 | 0 | 0 | 0 | 0 | 0 |
| PRNr | 0 | 0 | 0 | 0 | 0 | 0,000173743 | 0,000471434 | 0 | 9,41226E-05 | 0,001097865 | 0 | 0 | 0 | 0 | 0 | 0 | 0 | 0 |

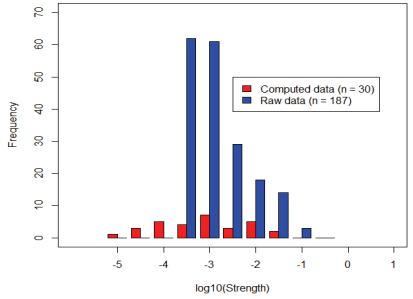

**Table S2 Results obtained in the analysis of dominating sets (Related to *Network density* in STAR Methods)**

| Targets | 1 | 2 | 3 | 4 |
|---|---|---|---|---|
| Nr of sets | 19 | 171 | 969 | 3876 |
| Dominated Size | Percentage of sets | | | |
| 0-10 | 0 | 0 | 0 | 0 |
| 10-20 | 0 | 0 | 0 | 0 |
| 20-30 | 0 | 0 | 0 | 0 |
| 30-40 | 0 | 0 | 0 | 0 |
| 40-50 | 0 | 0 | 0 | 0 |
| 50-60 | 0 | 0 | 0 | 0 |
| 60-70 | 0 | 0 | 0 | 0 |
| 70-80 | 0 | 0 | 0 | 0 |
| 80-90 | 10,53 | 0 | 0 | 0 |
| 90-100 | 21,05 | 8,77 | 0,41 | 0 |
| 100 | 68,42 | 91,23 | 99,59 | 100,00 |

**Table S3. ABI (anterograde), separated by injected vs. non-injected areas (Related to** *Partial coverage and global claims* **in STAR Methods)**

| Oh et al. indegrees | | | | | |
|---|---|---|---|---|---|
| *injected* | | | *non injected* | | |
| *name* | *in-degree* | *in-degree normalized (%)* | *name* | *in-degree* | *in-degree normalized (%)* |
| VISl | 10 | 76.92 | AUDpo | 11 | 78.57 |
| VISpl | 10 | 76.92 | VISpm | 11 | 78.57 |
| SSp.m | 11 | 84.62 | ORBm | 11 | 78.57 |
| VISal | 11 | 84.62 | RSPagl | 11 | 78.57 |
| VISam | 11 | 84.62 | RSPd | 11 | 78.57 |
| VISp | 11 | 84.62 | SSp.n | 12 | 85.71 |
| PTLp | 11 | 84.62 | ORBvl | 12 | 85.71 |
| AUDd | 12 | 92.31 | RSPv | 12 | 85.71 |
| AUDp | 12 | 92.31 | FRP | 13 | 92.86 |
| MOp | 13 | 100 | VISC | 13 | 92.86 |
| SSp.bfd | 13 | 100 | PL | 13 | 92.86 |
| SSp.tr | 13 | 100 | ORBl | 13 | 92.86 |
| SSs | 13 | 100 | MOs | 14 | 100 |
| TEa | 13 | 100 | SSp.ll | 14 | 100 |
| | | | SSp.ul | 14 | 100 |
| | | | SSp.un | 14 | 100 |
| | | | GU | 14 | 100 |
| | | | AUDv | 14 | 100 |
| | | | ACAd | 14 | 100 |
| | | | ACAv | 14 | 100 |
| | | | ILA | 14 | 100 |
| | | | AId | 14 | 100 |
| | | | AIp | 14 | 100 |
| | | | AIv | 14 | 100 |
| | | | PERI | 14 | 100 |
| | | | ECT | 14 | 100 |

**Table S4. SBRI outdegrees, ABI parcellation, separated by injected vs. non-injected areas (Related to *Partial coverage and global claims* in STAR Methods and Figure S3)**

| SBRI outdegrees, ABI segmentation | | | | | |
|---|---|---|---|---|---|
| *injected* | | | *non injected* | | |
| *name* | *out-degree* | *out-degree normalized (%)* | *name* | *out-degree* | *out-degree normalized (%)* |
| POR | 16 | 80 | SSp-nm | 14 | 66.67 |
| P | 17 | 85 | PM | 18 | 85.71 |
| AL | 18 | 90 | 36p | 19 | 90.48 |
| GU | 18 | 90 | LI | 20 | 95.24 |
| PD | 18 | 90 | LLA | 20 | 95.24 |
| A | 19 | 95 | ORBm | 20 | 95.24 |
| AUDpo | 19 | 95 | RSPv | 20 | 95.24 |
| LM | 19 | 95 | SSp-ul | 20 | 95.24 |
| MM | 19 | 95 | TEp | 20 | 95.24 |
| RL | 19 | 95 | ACAv | 21 | 100 |
| ACAd | 20 | 100 | AId | 21 | 100 |
| AM | 20 | 100 | AIp | 21 | 100 |
| ILA | 20 | 100 | AIv | 21 | 100 |
| MOp | 20 | 100 | AUDp | 21 | 100 |
| MOs | 20 | 100 | AUDv | 21 | 100 |
| PV | 20 | 100 | ECT | 21 | 100 |
| RSPd | 20 | 100 | ORBl | 21 | 100 |
| SSp-bfd | 20 | 100 | ORBvl | 21 | 100 |
| SSp-tr | 20 | 100 | PERI | 21 | 100 |
| SSs | 20 | 100 | PL | 21 | 100 |
| V1 | 20 | 100 | SSp-lj | 21 | 100 |
| | | | SSp-ll | 21 | 100 |
| | | | TEa | 21 | 100 |
| | | | UF | 21 | 100 |

**Table S5. SBRI outdegrees, present parcellation, separated by injected vs. non-injected areas (Related to** *Partial coverage and global claims* **in STAR Methods)**

| SBRI outdegrees, new segmentation | | | | | |
|---|---|---|---|---|---|
| *injected* | | | *non injected* | | |
| *name* | *out-degree* | *out-degree normalized (%)* | *name* | *out-degree* | *out-degree normalized (%)* |
| AL | 16 | 88.89 | PORa | 16 | 84.21 |
| P | 16 | 88.89 | SSp-nm | 16 | 84.21 |
| AUDpo | 17 | 94.44 | A | 18 | 94.74 |
| LM | 17 | 94.44 | FRP | 18 | 94.74 |
| PM | 17 | 94.44 | LI | 18 | 94.74 |
| RL | 17 | 94.44 | LLA | 18 | 94.74 |
| SSp-un | 17 | 94.44 | POR | 18 | 94.74 |
| ACAd | 18 | 100 | RSPv | 18 | 94.74 |
| AM | 18 | 100 | SSp-lj | 18 | 94.74 |
| DP | 18 | 100 | SSp-ul | 18 | 94.74 |
| GU | 18 | 100 | ACAv | 19 | 100 |
| MM | 18 | 100 | AId | 19 | 100 |
| MOp | 18 | 100 | AIp | 19 | 100 |
| PL | 18 | 100 | AIv | 19 | 100 |
| RSPd | 18 | 100 | AUDd | 19 | 100 |
| SSp-bfd | 18 | 100 | AUDp | 19 | 100 |
| SSs | 18 | 100 | AUDv | 19 | 100 |
| V1 | 18 | 100 | ECT | 19 | 100 |
| VISC | 18 | 100 | ILA | 19 | 100 |
| | | | MOs | 19 | 100 |
| | | | ORBl | 19 | 100 |
| | | | ORBm | 19 | 100 |
| | | | PERI | 19 | 100 |
| | | | RSPagl | 19 | 100 |
| | | | SSp-ll | 19 | 100 |
| | | | SSp-tr | 19 | 100 |
| | | | TEa | 19 | 100 |
| | | | TEp | 19 | 100 |